Texas A&M University
J. Mike Walker 66' Department of Mechanical Engineering
Turbomachinery Laboratory
Tribology Group

EXPERIMENTAL IDENTIFICATION OF FORCE COEFFICIENTS IN AN INTEGRAL SQUEEZE FILM DAMPER

TRC-SFD-1-19
Research Progress Report to the Turbomachinery Research Consortium

by

Xueliang Lu
PhD Candidate

Bonjin Koo
PhD Candidate

Luis San Andrés

Mast-Childs Chair Professor
Principal Investigator

Scott Tran

Undergraduate Research Assistant

May 2019

0

Executive summary

An integral squeeze film dampers (ISFD) offers the advantage of a lower number of parts, a shorter axial span, a lighter weight, split manufacturing, and higher tolerance precision Depending on the design requirement, an ISFD can be used to shift the rotor natural frequency to increase the operation safety margin between the running shaft speed and the critical speed; or to offer damping to enhance the stability of a rotor-bearing system. The reports details the results of an experimental and analytical endeavor to quantify and to predict the dynamic force coefficients of an ISFD. The test element has four arcuate film lands, 73° in arc extent, at a diameter of 157 mm. The film axial length equals 76 m and the clearance c is 0.353 mm. The lubricant is an ISO VG46 oil supplied at a low pressure (1 to 2 bar) and ~ 47 ^{o}C temperature. The damper has its ends sealed via end plates with a gap produced by an installed shim. Three sets are assembled with gaps equal to 0.53 mm. 0.43 mm and 0.28 mm. The measurements show the ISFD produces direct damping and inertia coefficients that increase with the static eccentricity albeit at a lower rate than predictions from the computational model ISFDFLEX®. The damper with the tightest sealed ends (gap =0.28 mm < c) shows 22 more damping that the open ends ISFD; however it also shows a significant (unexpected) stiffness hardening effect that contradicts the predictions. Added mass coefficients are significant for both the open ends ISFD and the sealed ends configurations with gaps 0.43 mm and 0.53 mm, This added mass coefficient exceeds the test element physical mass. ISFDFLEX® predicts well the damping coefficients, but largely under predicts the added masses. The experimentally estimated damping and inertia force coefficients offer relevant empirical evidence that strengthens prior art on ISFDs. As per predictions, the model produces accurate damping coefficients albeit the fluid inertia (virtual mass) coefficients are much lower than those obtained during the experiments.

Table of Contents

List of tables

List of Figures

Introduction

Squeeze film dampers (SFDs) aid to reduce amplitudes of rotor motion and improve rotor system stability while also allowing mehanical isolation of installed with elastic springs [1]. Common SFDs have a circular 360° film land geometry, as shown in Fig. 1, integrate either O-rings or piston rings as end seal elements, and are often mounted with an elastic cage for centering of a rotor. The squirrel cage stiffness can be tuned to place the rotor-bearing system critical speeds away from the operating speed range. However, the cage may requires a too large length, a detrimental factor in an aircraft engine application.
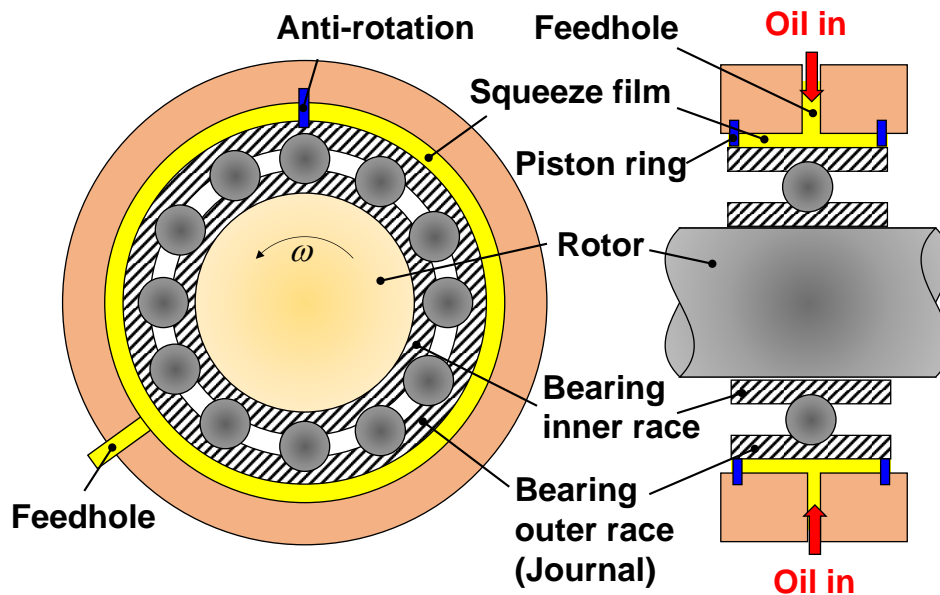
Fig. 1 Schematic view of a hole-fed circular SFD with end seals.

An integral squeeze film dampers (ISFD), as shown on the left graph on Fig. 2, offers the advantage of a lower number of parts, a shorter axial span, split manufacturing, higher tolerance precision, and (may be) a lighter weight, [2]. An electro discharge machining (EDM) manufacturing process produces individual arcuate damper film lands with *S*-shape flexural springs. The separate arcuate film lands act independently; hence an ISFD dynamic forced performance is quite distinct to that of a regular SFD. Note the film lands in an ISFD block the flow of lubricant in the circumferential direction. The right graph on Fig.2 shows a cross section view of the ISFD (not to scale) with the details of one of the film lands. The lubricant

enters through the inlet feed hole with pressure P_s, fills in the arcuate film land, and flows toward the two sides. End plates, with a small axial gap b_1 over a radial length l_1, seal the ends of the damper lands to create a large flow resistance. The lubricant flow exits radially outward and then turns axially (at the OD of plates) to discharge at ambient pressure P_a. The radial gap $b_2 < b_1$ while $l_2 << l_1$. The total <u>static</u> pressure difference through the ISFD is $\Delta P = P_s - P_a$.
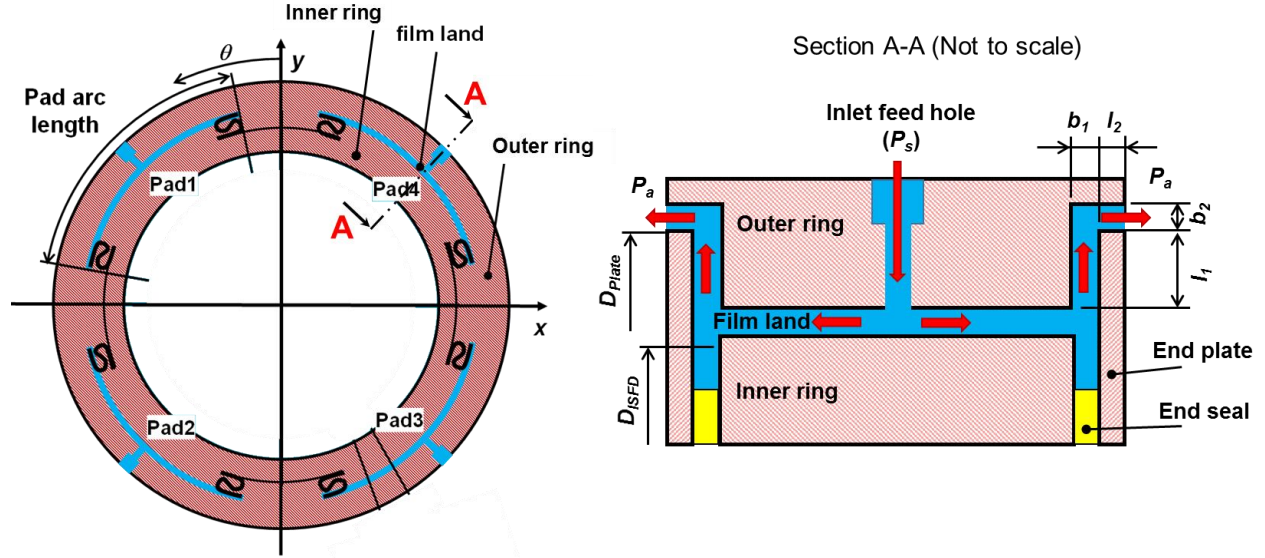
Fig. 2 (left) Schematic view of an ISFD with S-springs, (right) Cross section view showing lubricant flow path (not to scale).

Although ISFDs have been around for over 20 years, their application is limited to certain types of process gas compressors and as a drop-in retrofit to displace system critical speeds away from a certain operating speed range. In this last case, ISFDs offer mainly structural isolation. Application of ISFDs into aircraft engines has taken longer than usual, in spite of their significant advantages. Their time is ripe, however; as air breathing engine manufacturers search for ultra-short damper configurations ($L/D\sim0.2$), five to seven in a typical engine. The savings in axial space are a premium to shorten overly long, multiple shaft flexible rotors.

From classic lubrication theory [3], the damping (C) and inertia (M) force coefficients for a tightly sealed circular SFD and operating with a full film (no oil cavitation) condition are

$$C_{XX} = C_{YY} = 12\pi \mu L \left(\frac{D}{2c}\right)^3; \; M_{XX} = M_{YY} = \alpha \pi \rho \frac{L}{c}\left(\frac{D}{2}\right)^3 \quad (1)$$

6

where c is the film uniform radial clearance, L is the film axial length, D is the journal diameter, and (ρ, μ) are the lubricant density and viscosity. Above $\alpha \to 1.2$ for a small squeeze film Reynolds # $Re_s = (\rho/\mu)\omega c^2 \to 0$, and $\alpha \to 1.0$ as $Re_s \to \infty$. Here, ω denotes the frequency of journal whirl motion. The equations above are valid for small amplitude journal motions.

Note the analytical solution above does not account for the arcuate sector film lands as in an ISFD. For motions about a centered condition (null eccentricity e=0), De Santiago and San Andrés [2] introduce a simple expression for damping in an open ended ISFD with films of arc length β

$$C_{ISFD} = \pi \mu \left(\frac{L}{c}\right)^3 \left(\frac{D}{2}\right)\left(\frac{2\beta}{\pi}\right)^2 \tag{2}$$

De Santiago and San Andrés also predict ISFD damping force coefficients by solving the Reynolds equation using a finite element method [2]. No similar expression as Eq. (2) is available yet for added mass coefficients. In the mid 1990's, San Andrés and students [2-3] conducted imbalance response tests with a heavy three-disk rotor supported on ball bearings in series with ISFDs, and demonstrated their capability to produce viscous damping, amplified by the proper selection of end plate seals restricting the axial flow.

Much later in 2011, Delgado et al. [4] conduct dynamic load experiments with an ISFD having four 60° arcuate pads with clearance c=0.58 mm, diameter D= 169 mm and length L=44 mm. The S-spring stiffness equals 8.8 MN/m. End plates, extending 9.5 mm and with 25 µm gap, seal the axial sides of the damper lands. The authors find a test damping coefficient at about 50% of their prediction and a large virtual mass coefficient, one order of magnitude larger than the predicted virtual mass. Note that ISFD manufacturers typically ignore the (significant) virtual mass effect.

In 2012, Agnew and Childs [5] identify the force coefficients of a flexure pivot tilting pad bearing in series with an ISFD, see Fig. 3. The mechanical element could be used to control the support stiffness towards reducing system critical speeds. The four pads damper (73° arc length) has D=158 mm, L=76 mm, c=0.356 mm, and end plate seals with a large gap, 2.4 mm. The test results demonstrate the series mechanical device has a lower direct stiffness and added mass compared to those of the tilting-pad bearing alone. The experimentally estimated damping coefficient remains practically unchanged, however.
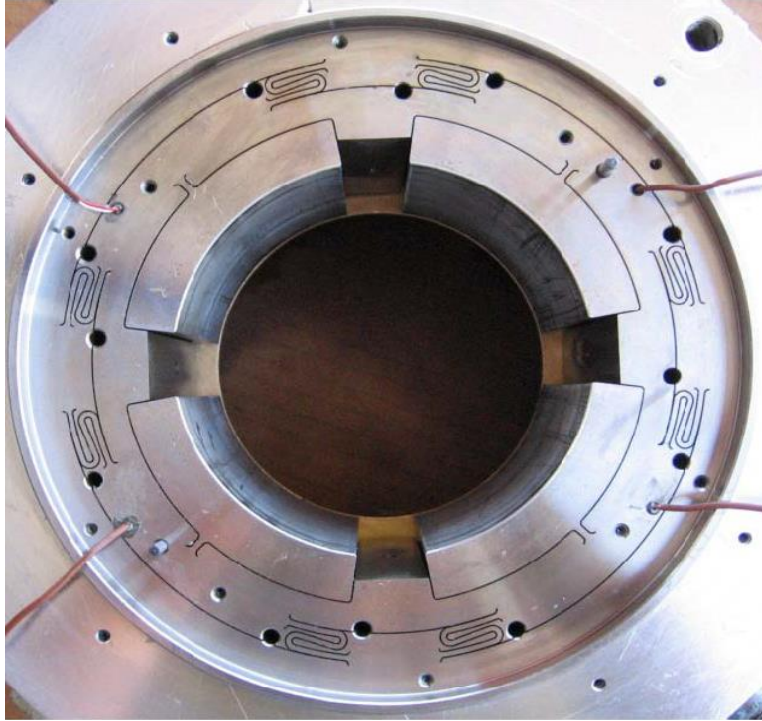
Fig. 3 Test ISFD in series with TPJB [5]. Damper lands at *D*=158 mm, *L*=76 mm, with clearance *c*=0.356 mm.

In 2018, Ertas et al. [6] report measured and predicted damping and inertia coefficients for an ISFD having a film clearance *c*=0.560 mm and hosting end plate seals with distinct gaps: 0.114 mm, 0.116 mm, 0.191 mm, and also open ends. The damper has four 54° arc film lands at diameter *D*=141 mm with axial lenth *L*=56 mm. S-springs at the arc ends have stiffness ~220 klb$_f$/in and connect to four short 19° arc film lands at a smaller diameter of 127 mm. Note the end seals' gap is smaller than the film clearance. ISO VG32 oil at 49°C and 2.4 bar is supplied thru orifices (ϕ=2 mm) at the center of each 54° arc film land. A finite element model solves the extended Reynolds equation for evaluation of the pressure field under squeeze film actions. As expected, the ISFD damping and inertia coefficients dramatically decrease as the end seal gap increases. The predicted added mass coefficients are thrice the test magnitude whereas the predicted damping coefficient correlates well with the experimentally derived force coefficient. The authors speculate the discrepancy is due to ignoring fluid inertia convective terms. Just as likely, the overly tight end seals not only restrict flow but also trap (incompressible) fluid in the arcuate film lands to amplify the test system inertia [7].

Objectives of TRC funded work in 2018-2019

The main objective is to further analysis and revamp a computational tool, legacy finite element (FE) code SFDFLEX®, for prediction of the dynamic performance of both SFDs[1] and ISFDs. The tool will include:

(a) Integration of elastic S-springs' stiffness for estimation of the static sag due to a load (a fraction of rotor weight) and the (change in) nominal film clearance for each of the arcuate film segments.

(b) Include an end plate seal coefficient based on its geometry (length and gap).

(c) Add sources of constant pressure such as a feedhole (orifice with flow resistance) or discharge hole.

(d) Solve the extended Reynolds equation including temporal fluid inertia effects and deliver ISFD force coefficients for (a) small amplitude motions about a static eccentric position. The coefficients will include the effective action of the S-Springs and damper (journal) mass.

(e) Use the tilting pad bearing test rig to accommodate the existing ISFD, see Fig.3, and conduct dynamic load tests to obtain ISFD force coefficients for ready comparison and validation of the model.

The following sections describe the test ISFD and test rig as well as the procedure for extracting force coefficients from dynamic load measurements. Next, the computational physics model is detailed along with comparisons against the current experimental results.

Description of test ISFD bearing

Figure 4 shows a schematic view and photograph of the test bearing comprising an inner section or ring with four flexure supported pads that make a tilting pad hydrodynamic bearing (TPJB) and an outer section or fixed ring with S-shaped flexures and narrow lands that make the integral squeeze film damper (ISFD). The TPJB and ISFD are in series, i.e. the load applied into the hydrodynamic bearing is transmitted to the ISFD. The single piece bearing is manufactured with a wire electro discharge machining (EDM) process. The test bearing is the same as that used by Agnew and Childs [5].

Agnew and Childs [5] test the TPJB-ISFD under conditions of unit load ranging from 172 kPa to 862 kPa, and shaft speeds from 4,000 rpm to 12,000 rpm. In the tests, the authors also shimmed the ISFD lands to demonstrate the operation of the TPJB alone.

---

[1] Note XLTRC[2]® includes too simplistic SFD codes, not updated since the PhD Dissertation of Dr. San Andrés in 1985.
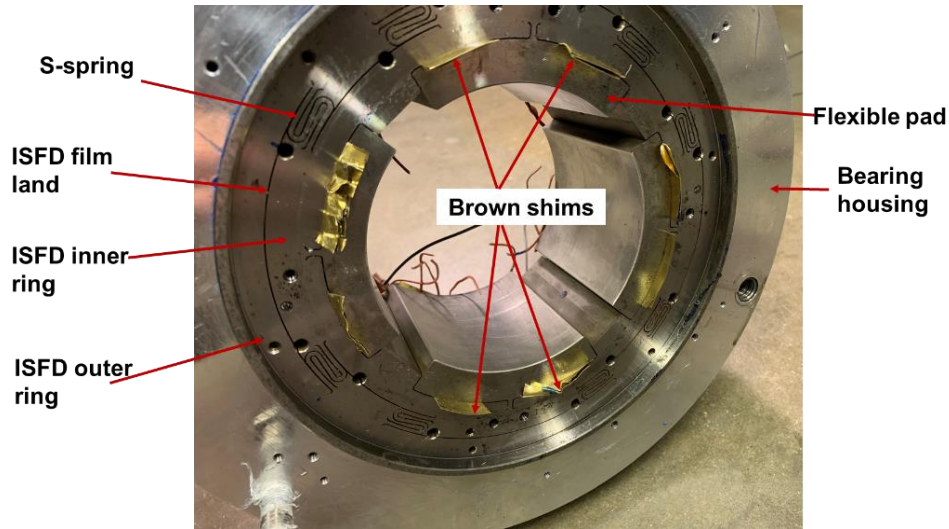
Fig. 4 Integral squeeze film damper with flexure tilting pads fixed with shims.

Presently, the tilting pads in the hydrodynamic bearing are shimmed and the bearing is installed without a clearance into a support stationary rigid shaft, as will be described later (see Fig. 6). In this manner, the experimental process aims to characterize the dynamic force response of the ISFD alone.

Table 1 shows the dimensions of the damper section of the test bearing and the lubricant physical properties. The ISFD has four film lands with an arcuate extent of 73° and located at a radius (½ D) = 78.5 mm. Each land has axial length (L) equal to 76 mm and the nominal radial clearance (c) is 0.356 mm (± 3 μm). Lubricant is supplied into the middle span of a film land through a supply orifice with diameter equal to 1.93 mm and a radial length equal to 3.96 mm. The test bearing and the attached housing weigh 19 kg.

During the experiments, an ISO VG46 oil lubricates the damper at a constant flow rate (Q) of 9.5 L/min. This flow rate corresponds to an inlet pressure between 1~2 bar(g), a typical hydrodynamic bearing supply pressure in an industrial compressor. The oil temperature is kept at 46 ±2 ˚C.

The damper ring has provisions for the installation of end plates that act as end seals. Figure 5 depicts a photograph of the damper and end plates that when fastened with an inner shim of known thickness (b_1) make a flow path for the lubricant leaving the damper lands. The configuration without end plates makes the lubricant discharge to ambient pressure, 1 bar(a). From here this configuration is named as open ends ISFD.

With the shims and flat arcuate plates fastened to the bearing ring, the flow resistance increases as the shim thickness (b_1) decreases[2]. Presently, tests are conducted with shims of thickness (b_1) equal to 0.53 mm (1.5 c), 0.43 mm (1.22 c), and 0.28 mm (0.78 c). That is, larger and smaller than the film clearance, c=0.356 mm.
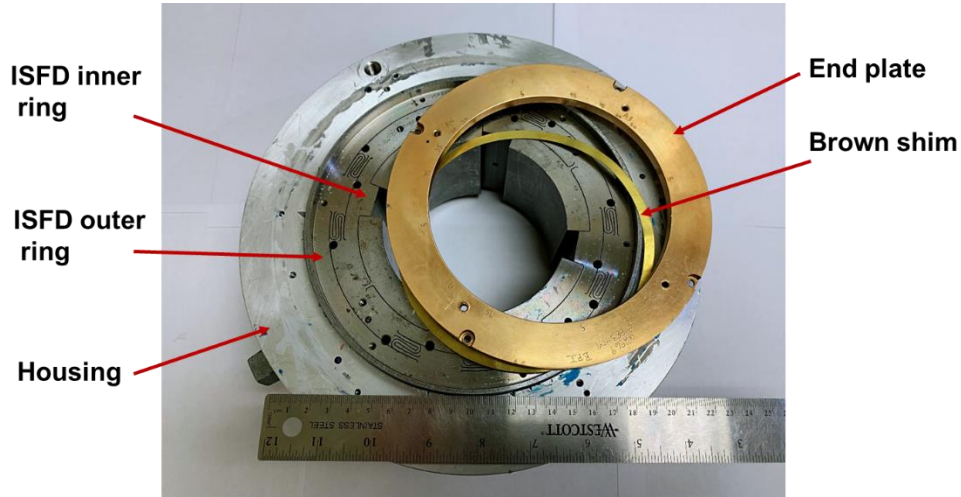
Fig. 5 Integral squeeze film damper, shim and end plate seal (tilting pads shims removed).

Table 1. Dimension of ISFD and fluid physical properties.

Diameter at film land, D_{ISFD}	157 mm (6.18 in)
Length, L	76 mm (3 in)
Film land clearance, c	0.356 mm (14 mil)
Number of pads, n	4
Arc radius, α	73°
Inlet orifice diameter, d_o	1.93 mm
Inlet orifice length, l_o	3.96 mm
End plate outer diameter D_{Plate}	172.5 mm
plate thickness, l_2	6.35 mm
Gap with bearing ID rim, b_2	0.85 mm
End seals clearance, b_1 (shim thickness)	0.28 mm, 0.43 mm, 0.53 mm, open end
radial length, l_1	7.75 mm
Load condition	Load between pad
ISO VG46 Viscosity, μ	31.2 cP (at 46 ºC)
Density, ρ	860 kg/m^3
Supply flow rate, Q	9.5 L/min (set pressure)

[2] The flow resistance from the end seals is the main source of damping for the said ISFD [6].

11

Description of test rig

Figure 6 presents a schematic diagram of the hydrodynamic bearing test rig [8] consisting of a main test-section supported on a steel bed plate, a rotor, and a driver air turbine motor. A 65 kW-power air motor drives the test shaft through a high-speed bellow coupling, a torque-limiter, and a torque meter. The maximum speed of the air turbine is 16,000 rpm. Presently, the air motor, meter and coupling are removed as the ISFD does not need these elements for its operation.

The test shaft is made from AISI 4140 material and machined to a precise diameter of 101.63 mm (3.9996 ± 0.0002 in.) at the test bearing section. Two angular contact ball bearings placed in a back-to-back orientation support the shaft. Two stiff pedestals hold the ball bearings, both being 406 mm (16 in) apart. An oil-mist lubrication system lubricates the ball bearings.

A pneumatic static loader applies a load only along the (-) y direction, whereas the hydraulic shakers apply dynamic loads along both the x and y directions as shown in Fig.7. A cable, connected to the bearing stator assembly through a pulley and a yoke, apply a static load along the (-) y-direction. A load cell, max. 22 kN, attached to the cable measures the applied load. The soft spring ($K_{spring} = 0.26$ MN/m) in the static loading system eliminates transmission of the vibration from the bearing stator to the static loader.

ITEM NO.	PART NO.
1	Test-rig pedestals
2	air turbine motor
4	Test rotor
5	Bearing stator
7	Collection Chambers
8	Static Loader Yoke
9	BedPlate
10	Pitch stabilizer bolts
11	Bellow Coupling
12	Torque meter (rotor)
13	Torque meter (stator)
14	Torque limiter
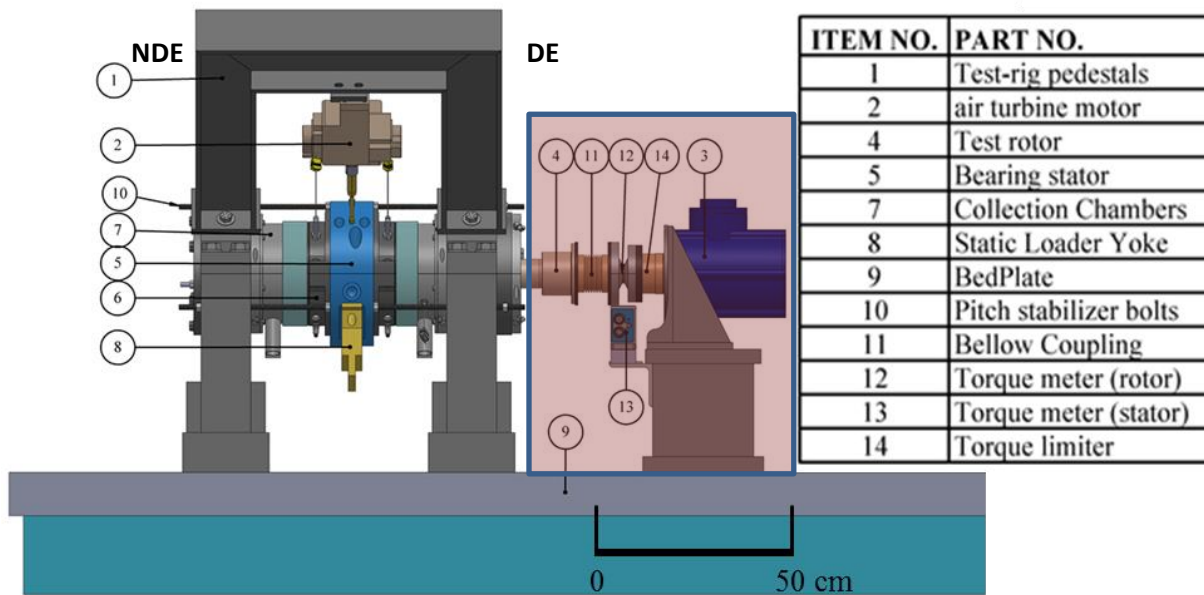
Fig. 6 Schematic diagram of test rig [8]. Air motor and coupling removed for tests with ISFD.

12

Two orthogonally mounted electro-hydraulic shaker heads attached to the bearing housing (stator) (a) deliver dynamic loads, and (b) aid to position the bearing relative to the shaft. Each shaker head consists of a hydraulic valve and a linear variable differential transformer (LVDT) sensor. A hydraulic-pump powers a shaker head, while an electronics master-controller precisely controls the stator static and dynamic motion. The shakers can exert a maximum load of 4.4 kN and excitation frequencies of up to 1 kHz. Along each direction (x, y), a stinger connects the shaker head to the bearing stator and transmits the static and dynamic load.

The current setup for the ISFD test does not include tensioned stabilizer bolts connecting the bearing stator to the pedestals. This is because the shaft does not spin and since the S-springs provide adequate support stiffness for the bearing housing.
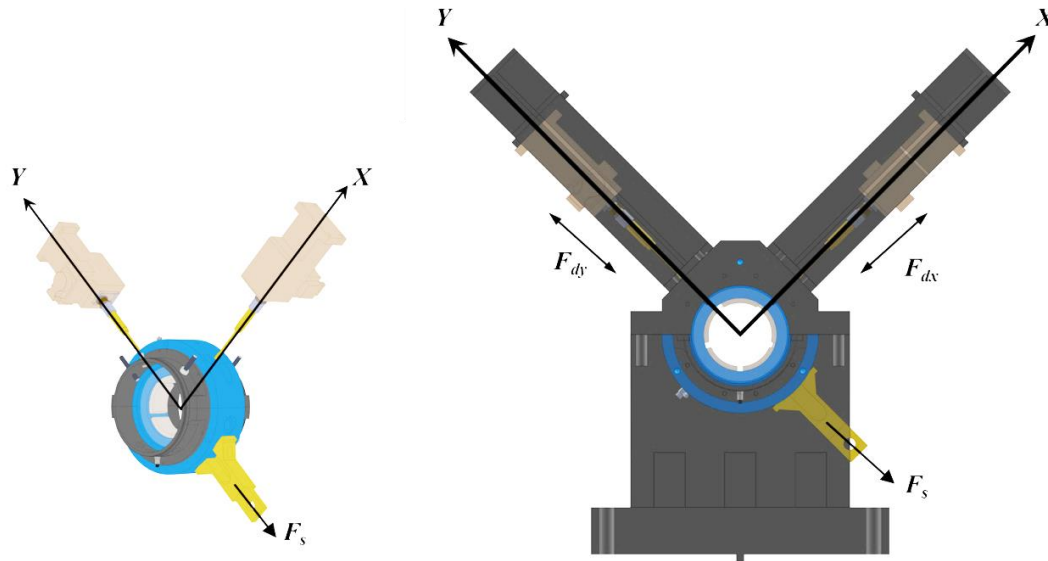
Fig. 7 (Left) Isometric and (right) front view from the NDE side of test rig loading arrangement [8].

Figure 8 shows the bearing stator that holds the test bearing, two end caps, and all the associated instrumentation. Four eddy-current sensors, located in the end caps, arranged in two mutually perpendicular directions measure the relative displacement between the shaft and bearing in x and y-axes. Two sets of the eddy-current sensors on each side of the test bearing allow monitoring of its pitch and yaw. Three J-type thermocouples measure oil temperature in the oil-inlet chamber as well as in the downstream end-caps. Three piezo resistive strain gauge-type pressure sensors installed on the bearing stator, and two end caps measure the oil pressure

13

at the inlet and outlet of the bearing, respectively.

Two force sensors mounted on the hydraulic shaker heads along the x and y directions measure the applied dynamic forces. One force sensor attached to the pneumatic static-loader cable measures the static load applied to the test bearing. Two accelerometers mounted on the bearing stator in the x and y-axes measure the acceleration of the bearing, respectively. A displacement sensor (not shown) facing the key phasor on the shaft measures the shaft angular speed. A turbine-type flow meter mounted upstream of the test rig measures the oil flow rate (max. 100 gpm) delivered to the test bearing.

Item no.	Part Name	Qty.
1	Bearing stator	1
2	Stinger	2
3	Static loader yoke	1
4	Bearing end caps	2
5	Load cell (force transducer)	2
6	Accelerometer	2
7	Pressure sensor	3
9	Thermocouple	3
10	Eddy-current sensor	4
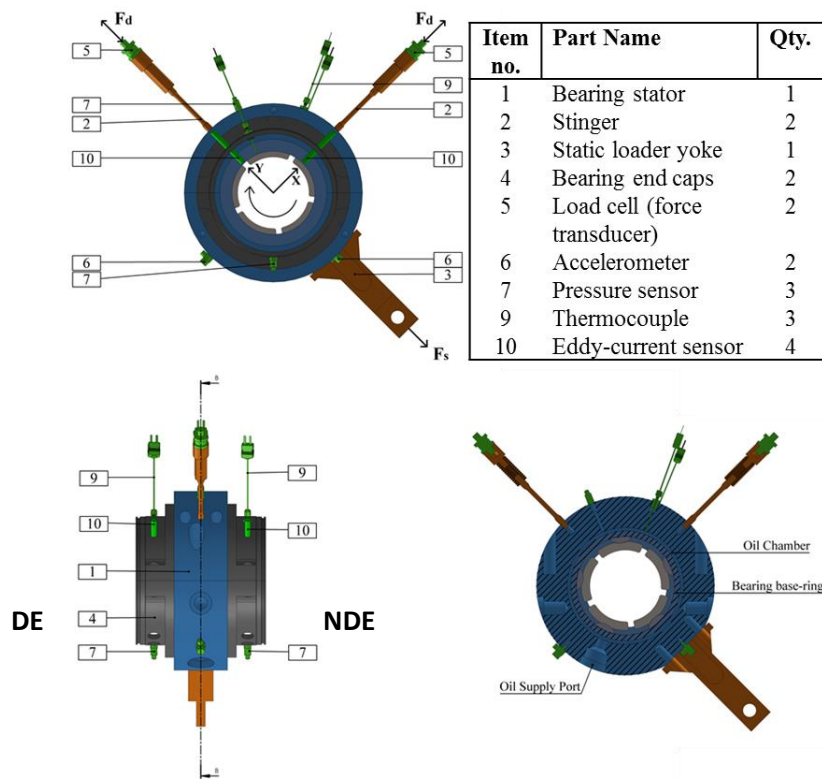
Fig. 8 Front view (top), side view (bottom left) and section view (bottom right) of bearing stator with instrumentation [8].

Figure 9 shows a photograph of the bearing test rig with the ISFD installed. The oil collectors on both sides of the ISFD are already in place. Presently, since the tests do not require shaft rotation, the test rig configuration is much simpler as the coupling and motor are not in place. The test ISFD bearing slides on the test rotor (with an interference). In this manner the bearing inner ring and constrained tilting pads become an integral part of the solid rotor.
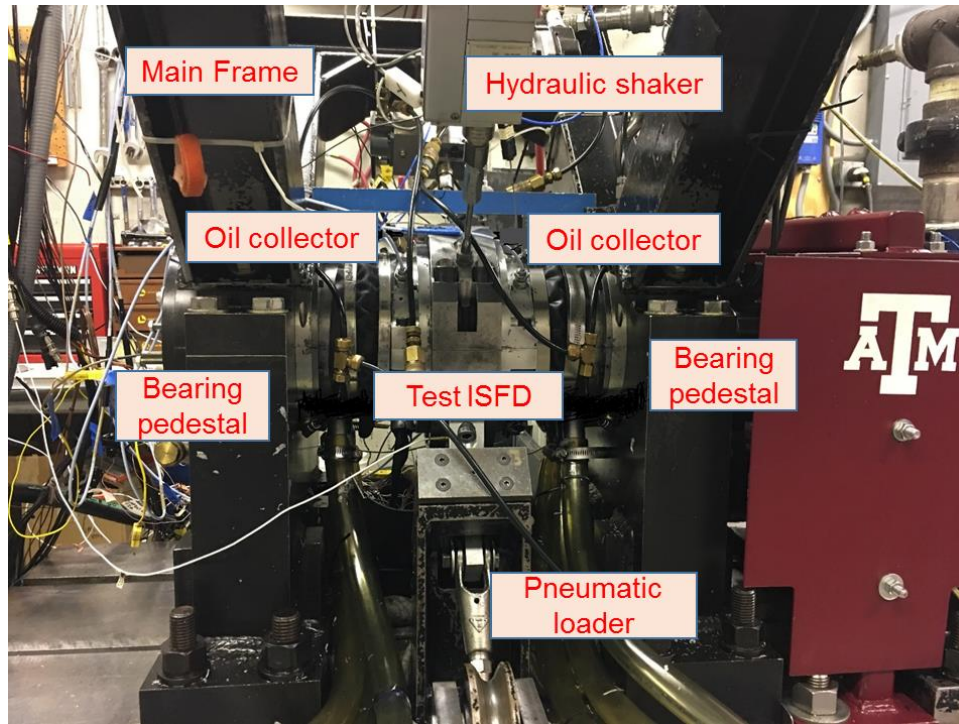
Fig. 9 Photograph of the ISFD bearing on the test rig.

Measurements of static displacement vs applied load and oil supply pressure for a constant flow rate

The ISFD bearing structure is installed to be statically loaded in between its pads (LBP). The hydraulic shaker[3] along the *Y* direction applies a static load and the two displacement sensors, one on each side of the ISFD housing, record the bearing static displacement along the same direction. Note the tests were conducted with the damper denuded of lubricant, i.e. under a dry condition.

Figure 10 shows the static load (*W*) versus bearing displacement or static eccentricity (*e*). The solid symbols represent the test data whereas the broken line stands for a linear curve fit, *W~ K_S e*. The slope of the line delivers the static stiffness 56.3 (±6) MN/m, representing the action of all the S-shaped springs connecting the damper lands to the ring.

Refer to Appendix A for measurements of the pair of S-shaped stiffness holding a pad. The magnitude found is *k*=38.8 MN/m.

---

[3] The hydraulic shaker operates in displacement control mode during the static load – displacement measurement.
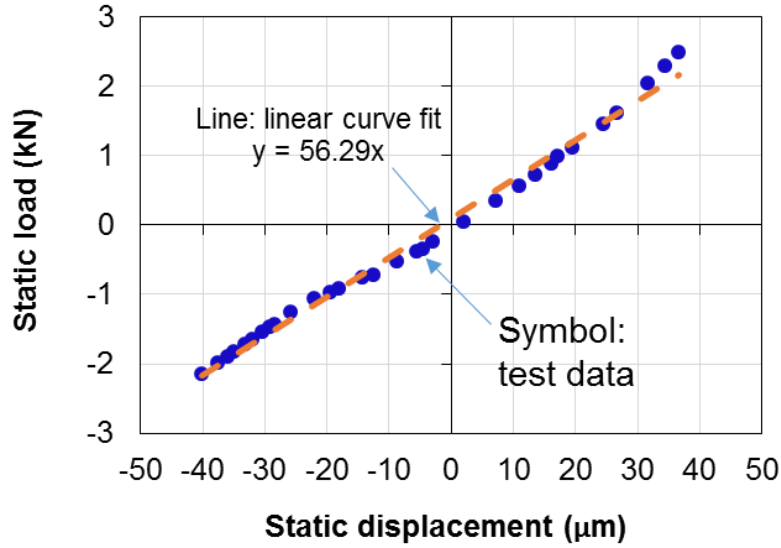
Fig. 10 Static load (*W*) versus displacement (*e*) conducted with dry ISFD. Tests for ISFD with open ends.

After the structural tests with the dry structure, lubricant is supplied to the ISFD for the various configurations built (end sealed). Table 2 lists the oil flow rate and pressure drop ($\Delta P = P_s - P_a$, see Fig. 2) recorded as the static eccentricity (*e*) increases due to a static load applied by the pneumatic cylinder. The inlet pressure shown in the table is a gauge pressure recorded in a feed groove (before the orifices into each land). Note for the open ends condition, the flow is relative low for *e/c* = 0.53 as the oil temperature is about 2 °C to 3°C lower than for the other cases. Since the experiments were conducted during the winter season, the oil temperature dropped quickly as the oil flowed through the pipe system.

Table 2 Recorded oil flow rate and supply pressure into ISFD vs. static eccentricity (e/c). Nominal clearance c=0.356 mm

	0.28 mm end seals			0.43 mm end seals			0.53 mm end seals			Open Ends		
e/c	Q_{in}	ΔP	T_{in}	Q_{in}	ΔP	T_{in}	Q_{in}	ΔP	T_{in}	Q_{in}	ΔP`	T_{in}
	LPM	bar	°C	LPM	bar	°C	LPM	bar	°C	LPM	bar	°C
0.0	9.5	1.8	46.4	9.5	1.3	46.5*	9.5	1.4	44.6	9.6	1.2	48.4
0.2	9.6	1.8	46.1	9.5	1.4	45.8	9.4	1.4	45.7	9.1	1.2	46.4
0.4	9.5	1.9	46.3	9.2	1.5	46.2	9.2	1.4	45.6	9.2	1.3	45.7
0.5	9.4	1.9	46.2	9.1	1.5	45.8	9.3	1.5	45.0	7.6	1.2	43.1
0.6	9.3	2.0	46.0	9.1	1.6	45.6	9.2	1.6	45.4	8.0	1.2	45.4
0.7	9.3	2.1	46.2	9.6	1.8	45.8	8.8	1.7	45.4	7.7	1.3	45.1

* $\mu = 31$ cP at 46.5 °C; $\mu = 34$ cP at 44.6 °C

16

Figure 11 shows the measured ISFD flow conductance $C_G = (Q/\Delta P)$ of the ISFD versus eccentricity ratio (e/c). The open ends configuration shows the largest C_G and reducing steadily by ~ 25% as the static eccentricity increases, $e/c \rightarrow 0.70$. The damper with the tightest end seals (b_1=0.28 mm) shows the lowest flow conductance, ~ 35% lower than that of the open ends configuration at the centered condition (e=0). Do realize C_G for the end seals with gap b_1=0.43 mm is larger than that for the 0.53 mm gap. This is due to the difference in inlet oil temperature. The lower the oil temperature, the larger the oil viscosity, and hence the lower C_G is.
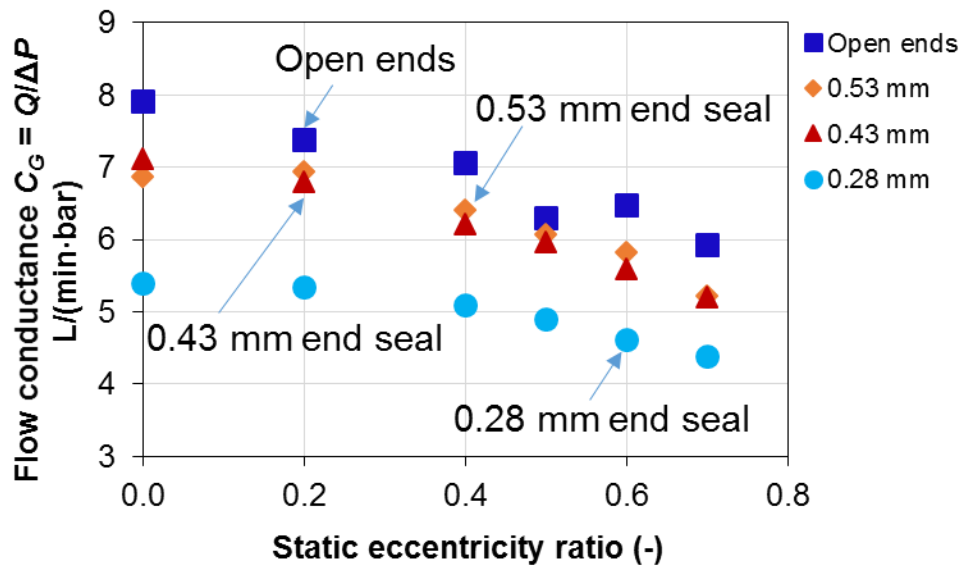
Fig. 11 Measured flow conductance (C_G) for test ISFD versus journal static eccentricity ratio (e/c). Tests for ISFD with open ends and configurations with end seals (gap b_1 varies).

Procedure for identification of force coefficients

During a dynamic load test, one shaker excites the bearing while the other shaker is at rest. The sampling rate is 10 k samples/s and the elapsed time for each shake is 32.768 s. The analysis software divides the data block into 10 sub-blocks, each containing 32,768 samples. The dynamic load contains multiple frequencies from 9.77 Hz to 166 Hz, in steps[4] of 9.77 Hz. For excitation along the X direction, the load cells record forces[5] $\mathbf{F}_{X(t)} = [f_{X(t)}, f_{Y(t)} = 0]^T$ applied

---

[4] The frequency 9.77 Hz is chosen to avoid the electric line frequency Hz and its multiples.
[5] ω is a set of frequency, and ω=(1, 2, 3,…, 17) · 9.77 Hz.

on the bearing, the eddy current displacement sensors record the housing displacement $Z_{X(t)}$[6] $= [X_{X(t)}, Y_{X(t)}]^T$ relative to the shaft, and two accelerometers record the absolute seal housing acceleration $A_{X(t)} = [a_{XX(t)}, a_{YX(t)}]^T$. After the excitation along the X direction stops, a shake along the Y direction follows. Similarly, the sensors record force $F_{Y(t)} = [f_{X(t)} = 0, f_{Y(t)}]^T$, displacements $Z_{Y(t)} = [X_{Y(t)}, Y_{Y(t)}]^T$, and accelerations $A_{Y(t)} = [a_{XY(t)}, a_{YY(t)}]^T$.

After an experiment ends, the time domain data is transformed into the frequency domain using Fast Fourier Transformation (FFT), i.e., $F_{X(\omega)} = $ FFT ($F_{X(t)}$). In the frequency domain, the matrices $F_{(\omega)} = [F_{X(\omega)} \mid F_{Y(\omega)}]$, $A_{(\omega)} = [A_{X(\omega)} \mid A_{Y(\omega)}]$, $Z_{(\omega)} = [Z_{X(\omega)} \mid Z_{Y(\omega)}]$ denote the applied forces, bearing housing accelerations and displacements, respectively.

In the frequency domain, the algebraic equations of motion for the test system lead to the estimation of a complex dynamic stiffness matrix (H) defined as

$$H(\omega) = [F(\omega) - M_S A(\omega)] \, Z^{-1}{}_{(\omega)} \tag{3}$$

where M_S is the bearing effective mass. Note that $H = (H_S + H_{ISFD})$ adds both the structure and ISFD force coefficients. Incidentally, the complex dynamic stiffness (H) does not include the effect of the test element mass x acceleration as this *force* is subtracted from the applied external force, as shown in Eq. (3).

The real part of the system complex dynamic stiffness (H) delivers the test system stiffness and mass coefficients (K, M), whereas the imaginary part produces the system damping (C) coefficients:

$$\text{Re}(H) \rightarrow K - \omega^2 M, \; \text{Ima}(H) \rightarrow i\,\omega\,C \tag{4}$$

Dynamic load excitations with the system *dry,* i.e. devoid of any lubricant, deliver a structure stiffness[7] $K_S = 60$ MN/m, system mass $M_S = 19$ kg, and damping $C_S = 13.5$ kN s/m. These parameters (K_S, M_S and C_S) are used as baseline data. The test *dry* system natural frequency is $f_n = 282$ Hz and its damping ratio $\xi_s \sim \dfrac{C_s}{2\sqrt{K_s M_s}} = 0.2$, a relatively large value for a typical mechanical structure (w/o lubricant).

Lastly, the (lubricated) ISFD force coefficients are estimated from

---

[6] Facing a specific direction (x and $y)$ there are two eddy current displacement sensors, one on each side of the test element, thus $Z_{X(t)}$ is the arithmetic average of two measured data. Both sensors deliver nearly identical displacements

[7] Note the *dry* static stiffness obtained from a dynamic load test (60 MN/m) is close to that obtained from a static load test (56.3 ± 6 MN/m). See Appendix B.

$$(\mathbf{K}, \mathbf{C}, \mathbf{M})\_ISFD = (\mathbf{K}, \mathbf{C}, \mathbf{M}) - (\mathbf{K}, \mathbf{C}, \mathbf{0})_S \qquad (5)$$

Experimental dynamic complex stiffnesses (*H's*) of test ISFD

For operation at a centered condition ($e=0$) and a supplied flow rate $Q \sim 9.5$ L/min, Figure 12 to Figure 15 show the real and imaginary parts of the system complex dynamic stiffness (**H**) versus frequency[8]. Each symbol represents an average of data collected from ten data sub-blocks, as described earlier. The error bar represents the standard deviation of each test variability[9]. The data shown includes results obtained from the dry structure alone, and the lubricated ISFD with open ends, as well as with end seals whose gap equals $b_1=0.53$ mm, 0.43 mm and 0.28 mm.

Figure 12 shows the real part[10] of H_{XX} and H_{YY} versus excitation frequency. For the structure alone, note $\text{Re}(H_{XX}) \sim \text{Re}(H_{YY}) = 60$ MN/m over the test frequency range. When oil is supplied to the ISFD, $\text{Re}(H_{XX})$ and $\text{Re}(H_{YY})$ decrease as the excitation frequency increases for both the open ends and the end seals configurations with $b_1=0.53$ mm (1.5 c) and $b_1= 0.43$ mm (1.22 c) gaps . The strong quadrature reveals a significant added (fluid) mass inertia effect.

On the other hand, for the configuration with the tightest end seal, $b_1=0.28$ mm (0.78 c), the dynamic direct stiffness is either constant ($\sim K_S$) or even increases with frequency. The test estimation seems quite odd! See Appendix B for more oddities. Incidentally, note the lubricated ISFD generates a slight negative stiffness as $\text{Re}(H_{XX})$ and $\text{Re}(H_{YY})$ are slightly lesser than K_S at the lowest frequency condition.

Figure 13 depicts the cross-coupled dynamic stiffnesses, *Re(H$_{XY}$)* and *Re(H$_{YX}$)* vs. frequency. Except for the condition with the tightest end seal, the cross-coupled stiffnesses are insignificant. The magnitudes obtained for the ISFD with *b* $b_1=0.28$ mm (0.78 c) point out to a structural coupling more than a fluid film effect, i.e. *Re(H$_{XY}$)* and *Re(H$_{YX}$)* have the same sign.

---

[8] Appendix B shows the system complex dynamic stiffness (*H*) versus frequency for operation with eccentricity form 0 to 0.7.

[9] The error bars do not appear in the graphs because of their small magnitude.

[10] These stiffness do not include the material mass of the steel bearing and its housing (M_S).
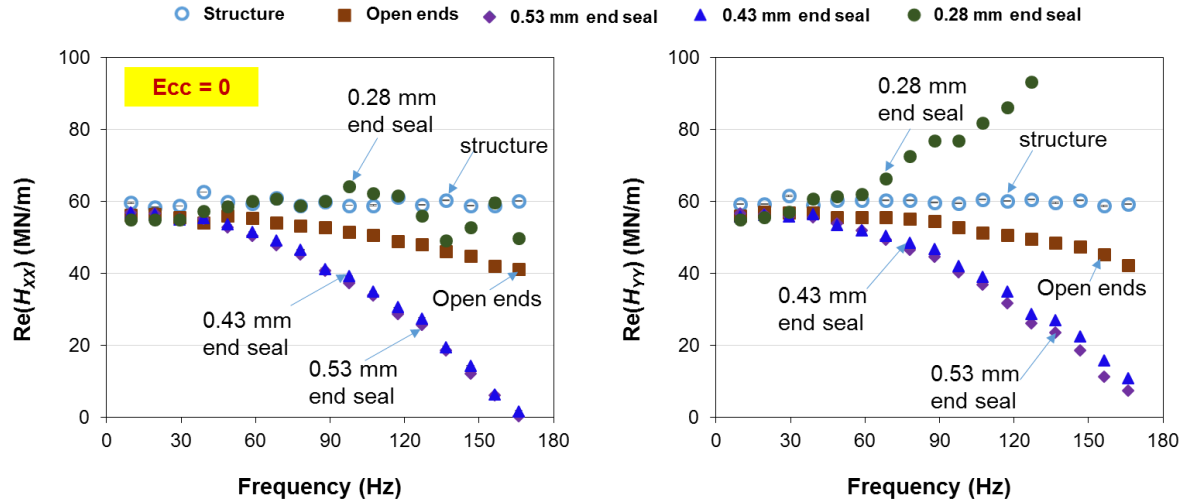
Fig. 12 Real part of dynamic complex system stiffnesses, Re(H_{XX}) and Re(H_{YY}), vs excitation frequency. Open and end sealed ends. Centered condition (e=0). Oil flow rate 9.5 L/min.
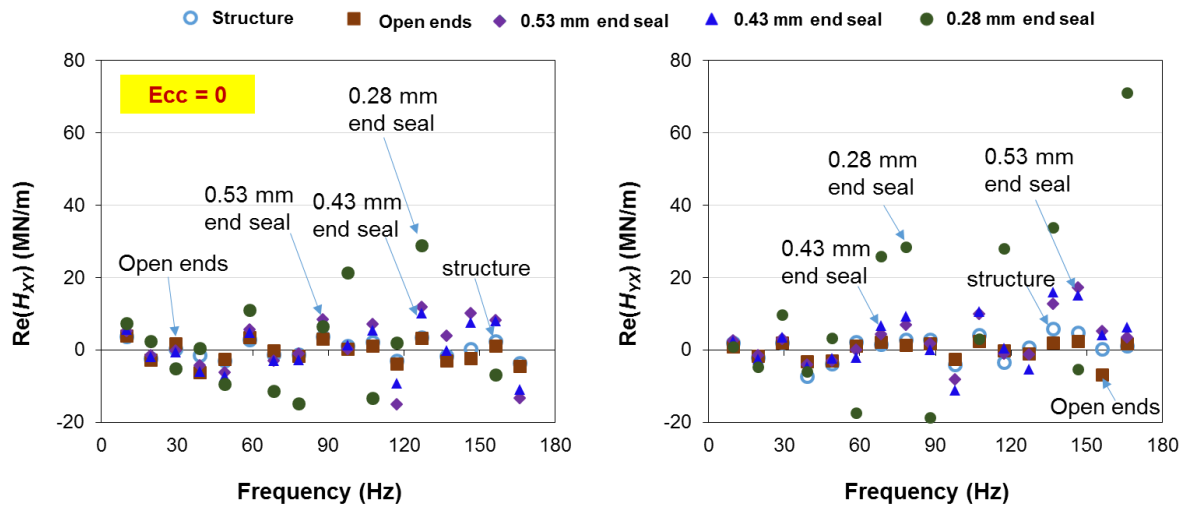
Fig. 13 Real part of dynamic complex system stiffnesses, Re(H_{XY}) and Re(H_{YX}), vs excitation frequency. Open and end sealed ends. Centered condition (e=0). Oil flow rate 9.5 L/min.

Figures 14 and 15 show the quadrature stiffnesses Ima(H), direct and cross-coupled, vs. excitation frequency, respectively. The cross coupled Ima(H_{XY}) and Ima(H_{YX}) are small in magnitude compared to the direct coefficients, hence unimportant to discuss. Note both Ima(H_{XX}) and Ima(H_{YY}) appear linear with excitation frequency thus the viscous model Ima(H) → $C\omega$ will reveal a very good correlation with the test results. When lubricated, the open ends

20

ISFD offers a little damping compared to that of the structure. However, the end seals effectively increase significantly the test element damping capability. Note the slope of Ima(H_{XX}) or Ima(H_{YY}) is the largest for the tightest end seal.

Fig. 14 Imaginary part of dynamic complex system stiffnesses, Ima(H_{XX}) and Ima(H_{YY}), vs excitation frequency. Open and end sealed ends. Centered condition (e=0). Oil flow rate 9.5 L/min.

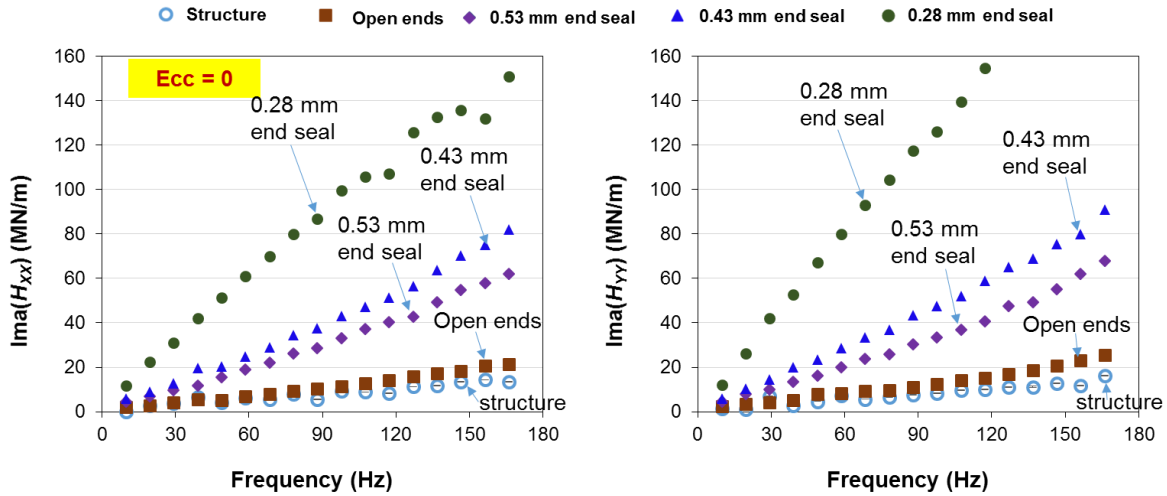**Fig. 15 Imaginary part of dynamic complex system stiffnesses, Ima(H_{XY}) and Ima(H_{YX}), vs excitation frequency. Open and end sealed ends. Centered condition (e=0). Oil flow rate 9.5 L/min.**
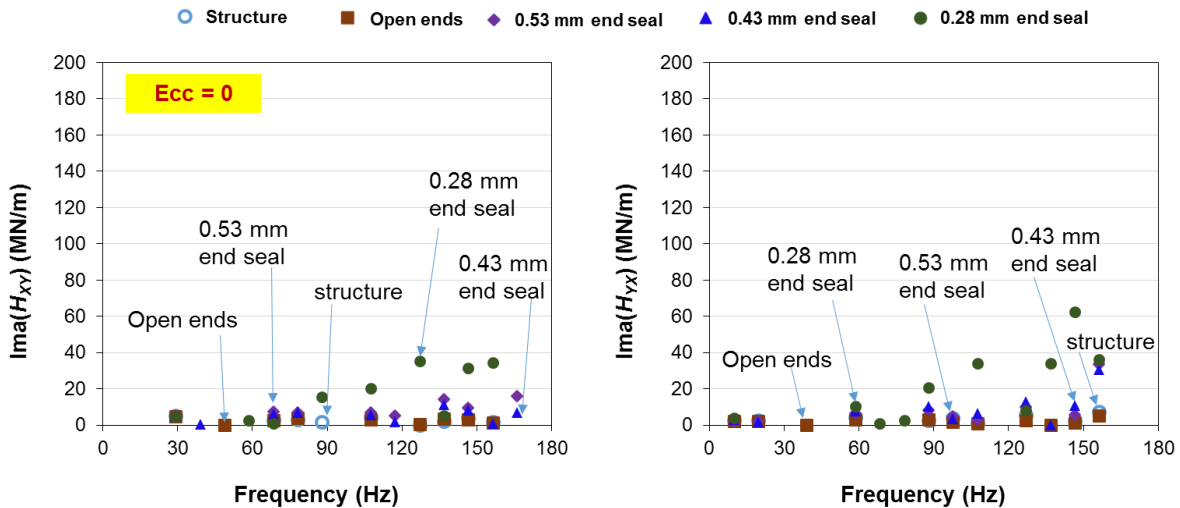
For operation at various off centered static conditions ($e>0$), Appendix B presents the real and imaginary parts of the system complex dynamic stiffness (**H**) versus excitation frequency. The behavior found for the various end seal conditions and at $e=0$ repeats for operation at a static eccentricity as large as 0.7. Note that for the tightest seals, Re(H) > 0 along X and Y directions. This evidences a strong hardening effect (negative virtual inertia).

Dynamic force coefficients for test ISFD

The ISFD direct force coefficients (stiffness $K_{\_ISFD}$, damping $C_{\_ISFD}$ and inertia $M_{\_ISFD}$) are obtained by subtracting the structural parameters from the system identified complex stiffnesses, see Eq. (5). Do note that cross-coupled force coefficients are insignificant for the most part and not further discussed. The force coefficients hereby presented are representative of the frequency range 9 Hz to 166 Hz.

Figure 16 show the ISFD film stiffnesses K_{XX_ISFD} and K_{YY_ISFD} versus static eccentricity ratio (e/c) for the various open and sealed ends configurations considered. Recall the static eccentricity is along the Y direction as determined from a pull load acting in between two adjacent pads. The film of the test damper generates a minor direct stiffness, negative in sign, when compared to that of its elastic structure, $K_S \sim 60$ MN/m.
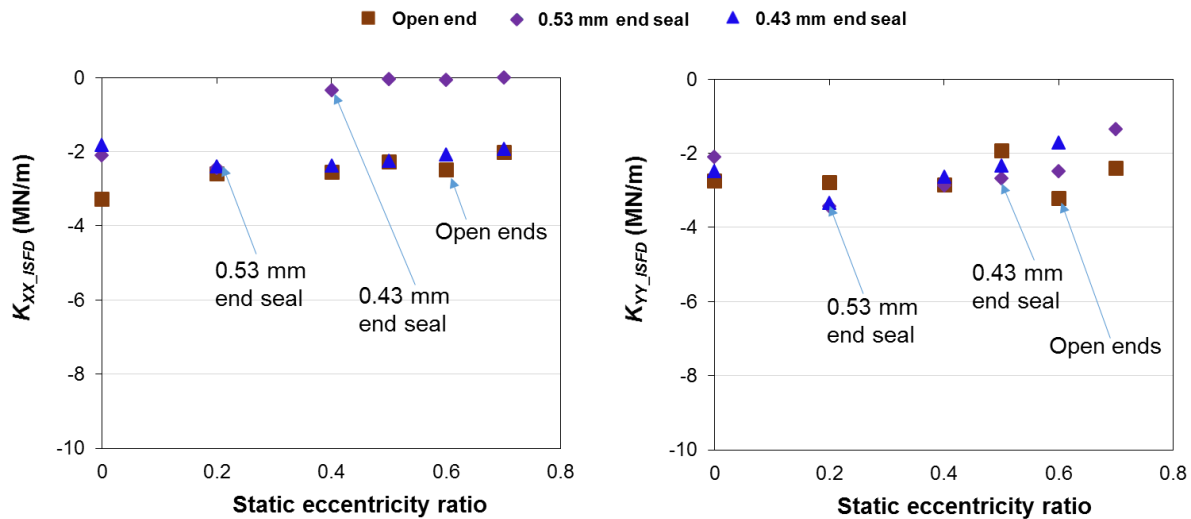
Fig. 16 Test ISFD film direct stiffnesses K_{XX_ISFD} and K_{YY_ISFD} vs static eccentricity ratio (e/c). Open ends and sealed ends with ends' gap b_1=0.43 mm and 0.53 mm.

Figure 17 show the ISFD direct added mass coefficients M_{XX_ISFD} and M_{YY_ISFD} versus the static eccentricity ratio (e/c) for the various configurations assembled. It is interesting to realize the mass coefficients are nearly constant and not particularly influenced by the applied static load (eccentricity e). Note the ends sealed ISFD with gaps b_1=0.43 mm and 0.53 mm shows nearly five time more added mass than the open ends ISFD. This finding is remarkable as the mass of the test structure (housing and ISFD) $M_S = 19$ kg. Note the mass coefficients along the Y direction are slightly larger than those along X, i.e., $M_{XX\_ISFD} < M_{YY\_ISFD}$, likely an effect of the static pull along the Y direction.

The results in Figs. 16 and 17 do not contain K_ISFD and M_ISFD coefficients for the ISFD sealed with the smallest gap b_1=0.28 mm (11 mil) $< c$ (=0.356 mm). Do recall the tightly sealed ends test element evidences a peculiar dynamic stiffness, see Fig 12 and Appendix A.
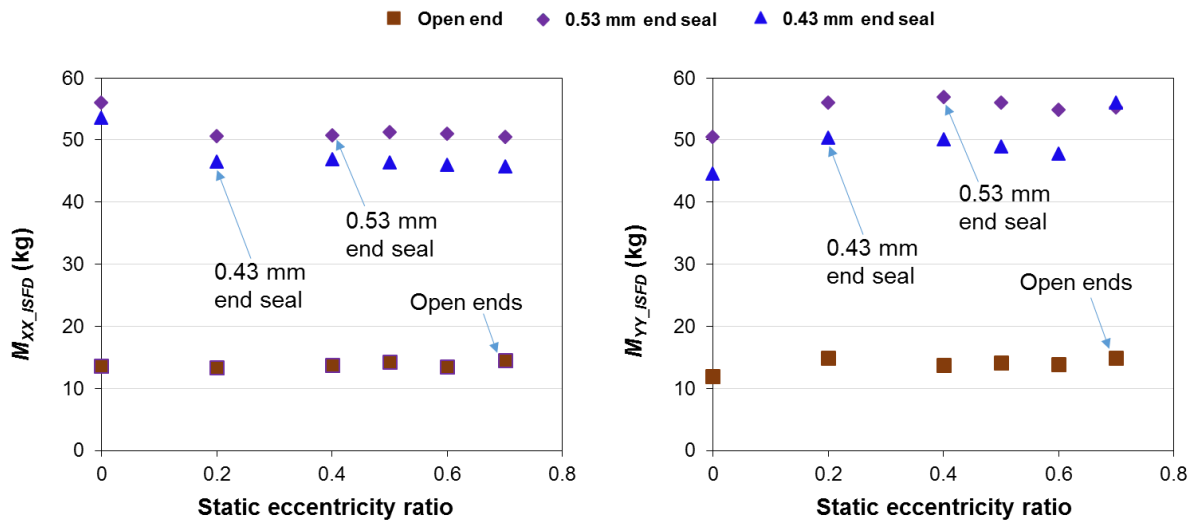
Fig. 17 Test ISFD direct fluid inertia coefficients M_{XX_ISFD} and M_{YY_ISFD} vs static eccentricity ratio (e/c). Open ends and sealed ends with end gap b_1=0.43 mm and 0.53 mm.

Figure 18 shows the ISFD damping coefficients C_{XX_ISFD} and C_{YY_ISFD} versus static eccentricity ratio (e/c) for the ISFD with open ends and the various end seals assembled configurations. Both C_{XX_ISFD} and C_{YY_ISFD} increase slightly with an increase in the static eccentricity. The open ends damper shows the lowest viscous damping while the configuration with the tightest end seal shows the most damping. In general, $C_{XX\_ISFD} \sim C_{YY\_ISFD}$ albeit for the tight clearance condition (0.28 mm), $C_{YY\_ISFD} >> C_{XX\_ISFD}$. The effect of the end seals' gap

(b_1) is remarkable as it substantially amplifies the damping magnitude generated by the mechanical element. From the open ends to the sealed ends ISFD, at $e=0$ (centered), the direct damping coefficient increases from 7,344 Ns/m to 44,223 Ns/m for gap $b_1 = 0.53$ mm, to 62,294 Ns/m for $b_1 = 0.43$ mm, to 164,305 Ns/m for $b_1 = 0.28$ mm. The damping increase is 22 times between the tight sealed ISFD and the open ends ISFD. Recall the ISFD diameter (lands) and axial length equal $D = 157$ mm and $L = 76$ mm; hence the damping coefficients, from open to sealed ends, should increase by $\sim [3\,(D/L)^2] = 12.8$. The difference is remarkable!

Differences in damping along the X and Y directions are due to the static load directed along the Y direction, as the static load causes a reduction in clearance on the side of the load direction (Y).
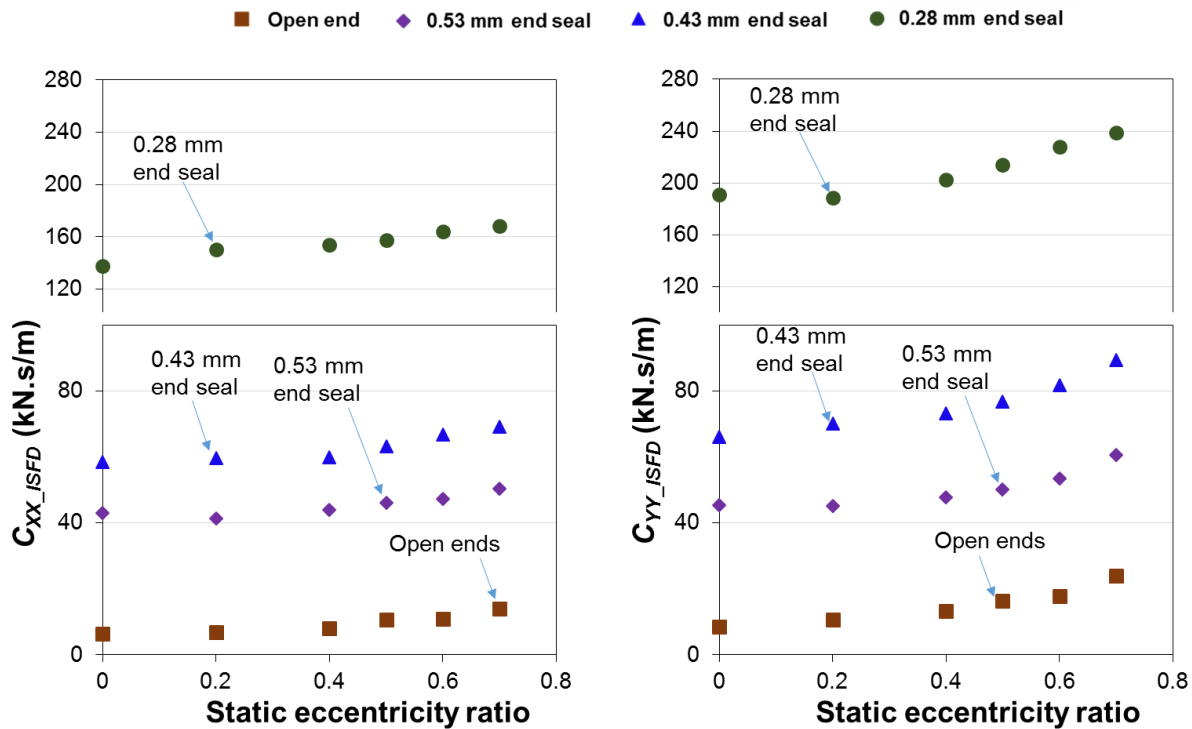
Fig. 18 Test ISFD direct damping C_{XX_ISFD} and C_{YY_ISFD} coefficients vs static eccentricity ratio (e/c). Open ends and sealed ends with end gap b_1=0.28 mm, 0.43 mm, and 0.53 mm. (Film clearance c=0.356 mm).

A model for the estimation of ISFD dynamic force coefficients

This section presents the numerical model for an ISFD and boundary conditions. The model is based on a prior numerical model introduced in Ref. [9]. The governing equation for the generation of the pressure field (P) in the film land is the extended Reynolds equation

$$\frac{\partial}{R\,\partial\Theta}\left(\frac{\rho h^3}{12\mu}\frac{\partial P}{R\,\partial\Theta}\right)+\frac{\partial}{\partial z}\left(\frac{\rho h^3}{12\mu}\frac{\partial P}{\partial z}\right)=\frac{\partial}{\partial t}(\rho h)+\frac{\rho h^2}{12\mu}\frac{\partial^2}{\partial t^2}(\rho h) \tag{6}$$

where h is the film thickness, and μ and ρ are the lubricant viscosity and density, respectively. Above

$$h=c+e_{sX}\cos(\Theta)+e_{sY}\sin(\Theta)+e^{i\omega t}\left[\Delta e_X\cos(\Theta)+\Delta e_Y\sin(\Theta)\right] \tag{7}$$

where c is the nominal film clearance, ω is the frequency, (e_{sX}, e_{sY}) denote the components of the journal static eccentricity along the X and Y directions, and $(\Delta e_X, \Delta e_Y)$ are the dynamic motion amplitudes with frequency ω.

In a perturbation analysis for small amplitude journal motions [9], the pressure is expressed as the superposition of a zeroth-order field (P_0) and first order components (P_X, P_Y). The components of the dynamic force follow from integration of the first order pressure field over the damper film lands as

$$\begin{Bmatrix}F_X\\F_Y\end{Bmatrix}=\begin{Bmatrix}H_{XX}+H_{XY}\\H_{YX}+H_{YY}\end{Bmatrix}\begin{pmatrix}\Delta e_X\\\Delta e_Y\end{pmatrix}=\int_0^{L_L}\int_0^{2\pi R}\left\{\left[e^{i\omega t}\{\Delta e_X\,P_X+\Delta e_Y\,P_Y\}\right]\begin{Bmatrix}\cos(\Theta)\\\sin(\Theta)\end{Bmatrix}dx\right\}dz \tag{8}$$

where $\left(H_{ij}=K_{ij}-\omega^2 M_{ij}+i\omega C_{ij}\right)_{\_ISFD}$ $i,j=X,Y$, respectively, with $(K, C, M)\_{ISFD}$ as the damper force coefficients.

In contrast to a conventional circular SFD, the pressure field in an ISFD is neither continuous nor periodic in the circumferential direction. Hence, one film land requires boundary conditions at the axial mid-plane, the axial ends, and the circumferential ends of the arcuate film.

Boundary condition on damper circumference. As shown in Fig. 19 for an arcuate film land, when an arc end blocks the flow, then $q_\theta \sim \dfrac{\partial P}{\partial\theta}=0$.
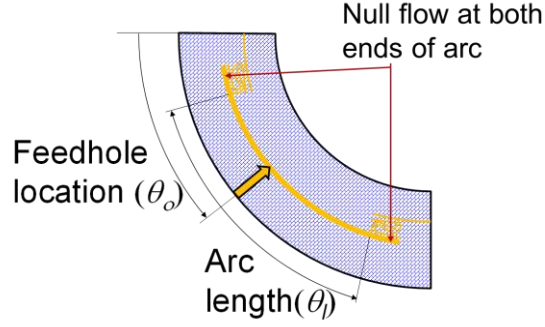
Fig. 19 A schematic view of a single arcuate film land with no circumferential flow at its ends.

Boundary conditions on axial ends and definition of end seal flow conductance

Figure 20 (top) illustrates a schematic view of the flow path through one arcuate film of the test ISFD sealed with two plates of thickness $l_2 = 6.35$ mm and outside diameter $D_{Plate} = 172.5$ mm. Fig. 20 (bottom) is a simplified view of the hydraulic network for the steady flow. The lubricant at supply pressure (P_s) enters each individual arcuate film through an orifice with flow resistance (R_o). After flowing through the orifice, the pressure reduces to $P_{(z=0)} = P_i$. Due to axial symmetry, half of the lubricant flows axially through the right hand side of the film land, each with resistance (R_f), and exits at $z = \frac{1}{2} L$ at pressure $P_{(z=\frac{1}{2}L)} = P_e$. Lastly, the flows (four) exiting the right side of each arcuate film land merge and exit after passing through the end plate seal with resistance (R_s) to ambient pressure (P_a). The flow through the left side of the film land follows a similar path.

Along the axial mid-plane ($z=0$), the axial flow is null ($q_z=0$) due to symmetry. The film axial ends ($z=\pm\frac{1}{2} L$) can be either sealed or open. For an open end, the lubricant exit pressure is ambient (P_a). For a sealed end, the axial flow (q_{1z}) per unit circumferential length through the end seal is proportional to the local pressure drop and a local flow conductance C_{seal}, i.e.,

$$q_{1z}\big|_{\theta,z=\frac{1}{2}L} = -\frac{h^3_{\left(\theta,z=\frac{1}{2}L\right)}}{12\mu}\frac{\partial P}{\partial z}\bigg|_{\theta,z=\frac{1}{2}L} = C_{seal}\left(P_e - P_a\right) \tag{9}$$
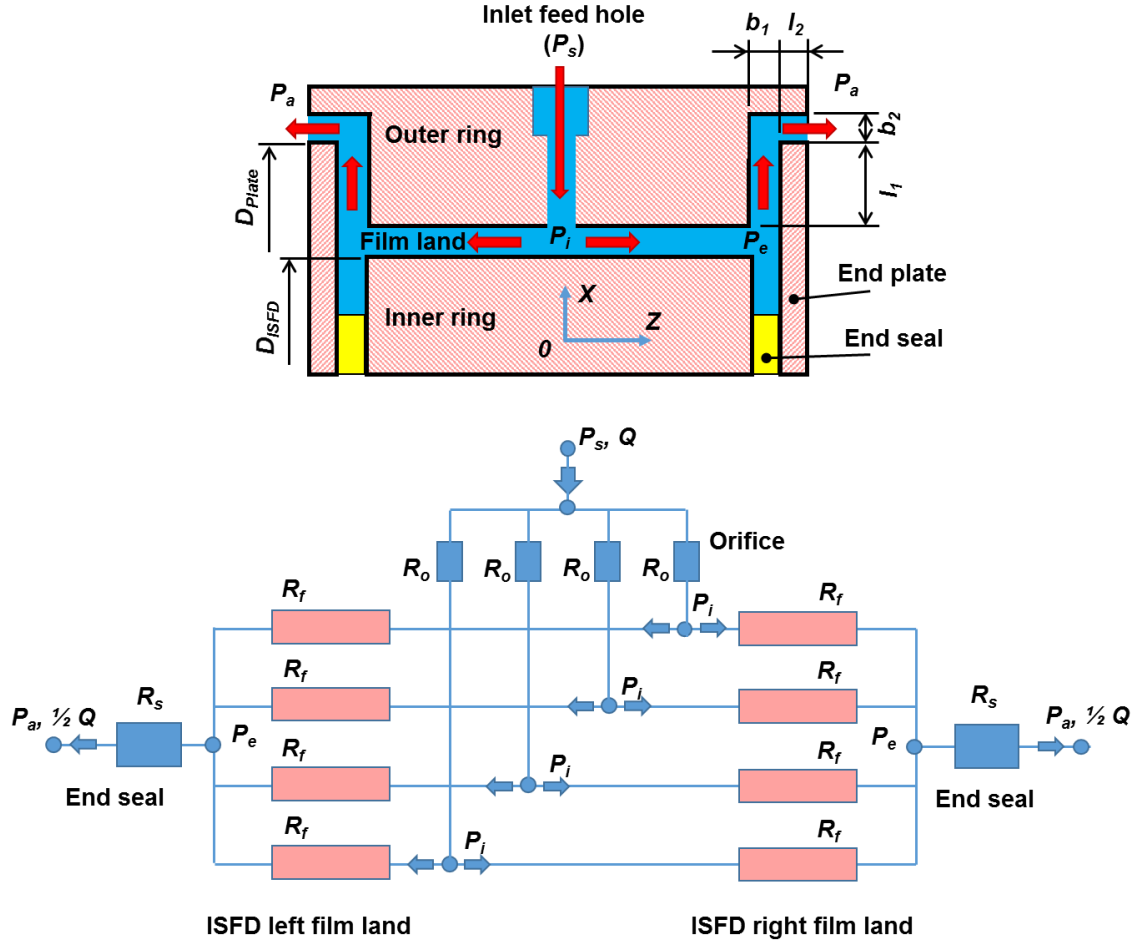
Fig. 20 (top) Schematic view of an ISFD with an end plate seal. l_1 = 7.75 mm, b_1 = 0.53 mm, 0.43 mm, and 0.28 mm, l_2 = 6.35 mm, b_2 = 0.85 mm. D_{ISFD}=157 mm, D_{plate}=172.5 mm. **Orifice diameter and length = 1.93 and 3.96 mm. (bottom) Network of flow resistances in an ISFD.**

A simple laminar flow analysis produces the local flow conductance per unit circumferential length

$$C_{seal} = \frac{1}{12\mu\left(\dfrac{l_1}{b_1^3} + \dfrac{l_2}{b_2^3}\right)} \sim \frac{b_1^3}{12\mu l_1} \tag{10}$$

Since $\dfrac{l_1}{b_1^3} > \dfrac{l_2}{b_2^3}$.

Integration of the end axial flow around the circumference delivers the total flow rate (two sides) as

$$Q = 2 \int\limits_{0}^{2\pi} q_{1z}\Big|_{\left(\theta, z=\frac{1}{2}L\right)} R\, d\theta \sim C_G \left(P_s - P_a\right) \tag{11}$$

Substituting Eq. (9) into (11) renders

$$Q = 4\pi\, R C_{seal}\left(P_e - P_a\right)\left[\frac{73}{90}\right] \tag{12}$$

where the film arc length (73°) is introduced in the formula. In Eq. (12), the end seal radius R increases from ($R_{ISFD} = \frac{1}{2}\, D_{ISFD}$) to ($R_{Plate} = \frac{1}{2}\, D_{Plate}$), thus a reasonable approximation is to set $R = \frac{1}{2}\,(R_{ISFD} + R_{Plate})$. Hence, Eq. (12) gives

$$C_G = \frac{Q}{\left(P_e - P_a\right)} = \pi \left(D_{ISFD} + D_{Plate}\right)\left[\frac{73}{90}\right]\frac{b_1^3}{12\,\mu l_1} \tag{13}$$

Above C_G is the global end seal flow conductance (includes two end seals).

Recall Table 2 lists the experimentally recorded ISFD supply flow rate (Q) and pressure difference (ΔP). Dividing the recorded pressure difference by the supply flow rate renders the ISFD global flow resistance (R_1). The hydraulic network graph in Fig. 20 (bottom) shows that the ISFD global resistance (R_1) is the summation of the orifice resistances (4 x R_o), the film lands flow resistances (4 R_f), and the two end seals flow resistance (2R_s), i.e.,

$$R_1 = \Delta P/Q = [\ 4\ R_o/4 + 4\ R_f\ ] +\ 2\ R_s \tag{14}$$

For the open ends condition, $R_s = 0$. Thus the end seals flow resistance can be obtained by subtracting the ISFD global resistance (R_1) for the open ends condition from that recorded with flow once the end seals are in place. That is,

$$2\ R_s = (R_1)_{\text{sealed}} - (R_1)_{\text{open}} \tag{15}$$

Then the end seals global conductance (C_G) is the inverse of the global end seal resistance.

$$C_G = 1/(2R_s) \tag{16}$$

Table 3 lists the end seals flow conductance (C_G) obtained Eq. (13) and from the flow vs. pressure measurements. The difference in C_G between prediction and measurements is large. The authors presume there in an error in the measurement of the supplied oil flow rate.

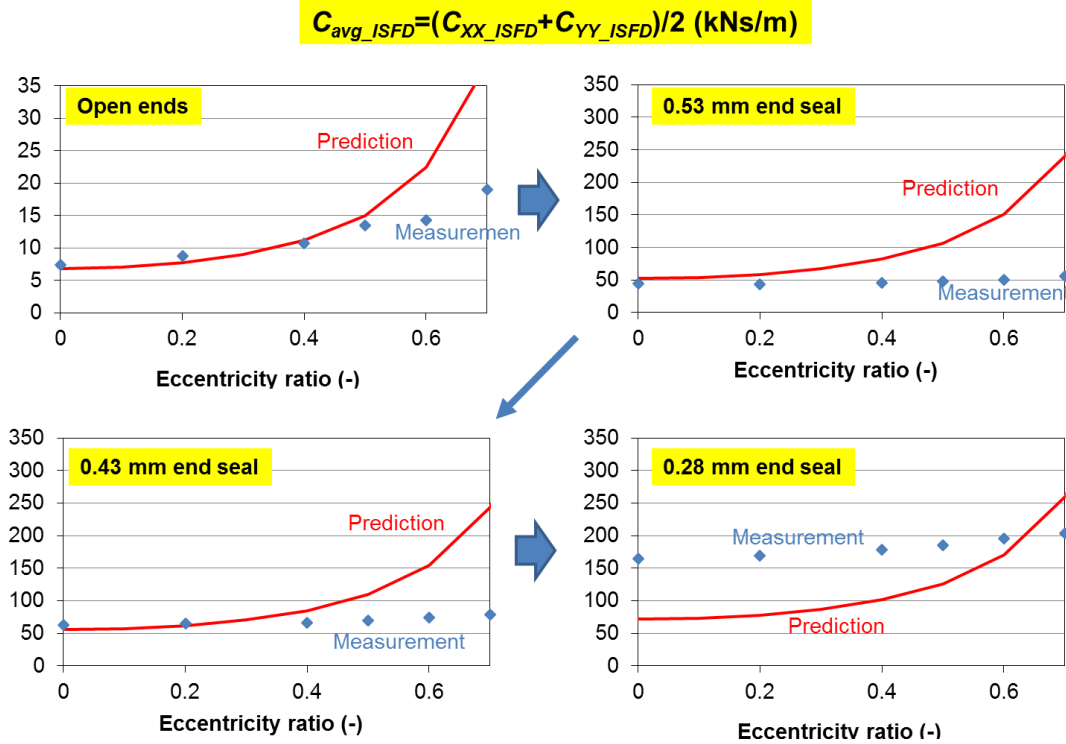**Table 3 Predicted and experimentally estimated end seals' flow conductance (static eccentricity = 0.2 x c)**

end seal gap, b_1	C_G from Eqn. (13) $10^{-9} \times$ m^3/(s Pa)	C_G From measurement $10^{-9} \times$ m^3/(s Pa)
0.28 mm	6.35	3.22
0.43 mm	23.0	14.6
0.53 mm	43.1	20.0

Predicted vs. experimental ISFD force coefficients

The computational model ISFDFLEX® predicts the ISFD force coefficients for the same static operating conditions (supply flow) as in the tests. Appendix C shows the graphic user interface (GUI) for the ISFD predictive tool: input data.

Figures 21 to 22 show predictions of the current model vs. the extracted physical force coefficients. For simplicity, the data shown on the graphs are averaged along the two directions, i.e., C_{avg}=0.5 (C_{XX}+C_{YY}).

Figure 21 shows the predicted and measured damping coefficients (C_{ISFD}) versus the static eccentricity ratio. In general the model predicts well the damping coefficients for the open ends configuration as well as most of the sealed ends configurations. The discrepancy between the prediction and the measurement increases as the end seal clearance reduces (smaller flow conductance). For the tightest end seals condition (b_1= 0.79 c), the measured damping is approximately twice as large as the predicted one. Note for both the open ends condition and the sealed configuration, both prediction and test show an increase in damping as the static eccentricity ratio (e/c) increases from 0 to 0.7.

$$C_{avg\_ISFD}=(C_{XX\_ISFD}+C_{YY\_ISFD})/2 \text{ (kNs/m)}$$

Fig. 21 ISFD damping coefficients (C_{ISFD}) versus static eccentricity ratio (*e/c*): predictions and measurements. ISFD with open ends and sealed ends with gap b_1=0.53 mm, 0.43 mm, and 0.28 mm.

Figure 22 shows the predicted and experimentally identified added mass coefficients (M_{ISFD}) versus static eccentricity ratio (*e/c*). The test derived added mass coefficients are well above the predicted magnitudes for all the test conditions. Note for the tightest gap configuration, the test data produces a negative mass coefficients as the complex dynamic stiffness increases with frequency, as shown by the real part of the dynamic stiffness in Figure 12. On the other hand, the prediction delivers a large mass coefficient.

$$M_{avg\_ISFD}=(M_{XX\_ISFD}+M_{YY\_ISFD})/2$$
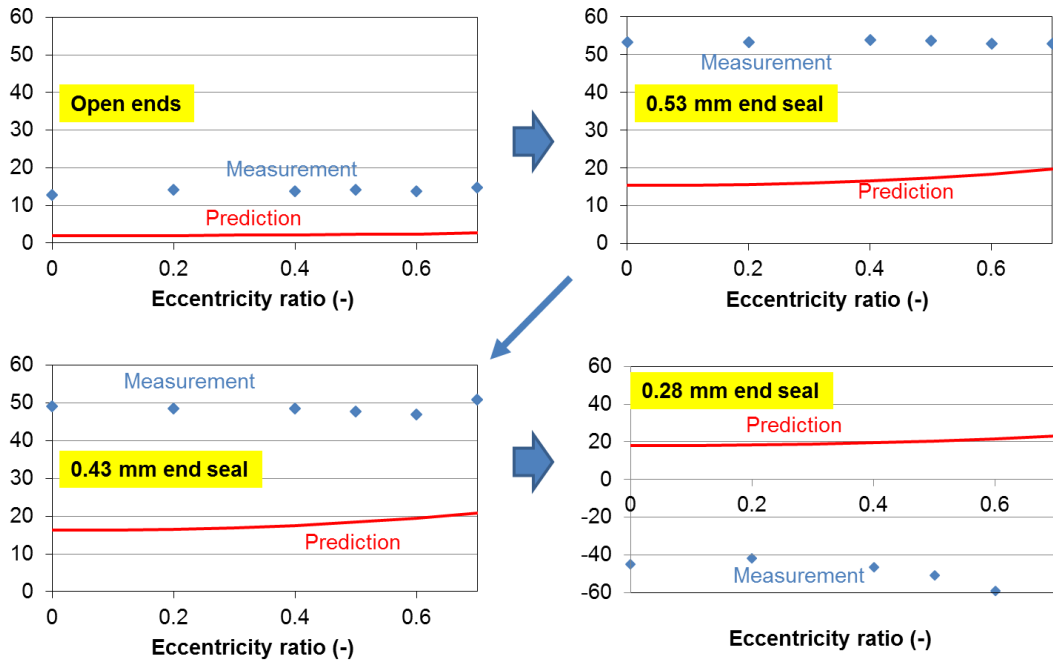
Fig. 22 ISFD virtual mass coefficients versus static eccentricity ratio (e/c): predictions and measurements. ISFD with open ends and sealed ends with gap b_1=0.53 mm and 0.43 mm.

Table 4 shows the recorded and predicted oil flow rate for operation with a centered condition (e=0, no static load). The table also shows the recorded (supply-discharge) pressure difference across the ISFD. Note the recorded oil flow rate remains rather constant at ~ 9.5 LPM. On the other hand, the predicted flow rate shows a constant reduction in magnitude as the end seal condition varies from open ends to one with a 0.28 mm gap. The source of the differences is to be asserted.

Table 4 Recorded and predicted oil flow rate. Static eccentricity (e/c=0).

	Sealed						→			Open		
	0.28 mm end seals			0.43 mm end seals			0.53 mm end seals			Open Ends		
Operation condition	ΔP	T_{in}	μ_{in}	ΔP	T_{in}	μ_{in}	ΔP	T_{in}	μ_{in}	ΔP	T_{in}	μ_{in}
	bar	ºC	cP	bar	ºC	cP	bar	ºC	cP	bar	ºC	cP
	1.8	46.4	31.2	1.3	46.5	31.2	1.4	44.6	34.1	1.2	48.4	28.1
Prediction (LPM)	2.1			4.7			8.1			6.9		
Measurement (LPM)	9.5			9.5			9.5			9.6		

Closure

Integral squeeze film dampers, when compared to conventional SFDs, offer the advantages of a lower number of parts, a shorter axial span, split manufacturing, higher tolerance precision, and (may be) a lighter weight. Depending on the design requirement, an ISFD can be used to shift the rotor natural frequency to increase the operation safety margin between the running shaft speed and the critical speed; or to offer damping to enhance the stability of a rotor-bearing system.

The current research investigates experimentally and analytically the dynamic forced performance of a test ISFD having four arcuate film lands, 73° in arc extent, at a diameter of 157 mm, and with axial length equal to 76 m and film clearance c=0.353 mm. The lubricant is an ISO VG46 oil supplied at a low pressure (1 to 2 bar) and ~ 47 ^oC temperature. The damper has its ends sealed via end plates with a gap produced by an installed shim. Three pairs of shim were used with thickness equal to 0.53 mm. 0.43 mm and 0.28 mm.

The analysis of the dynamic load measurements conducted over a range of static journal eccentricities leads to the following conclusions:

1. The ISFD does not produce a direct stiffness coefficient except for the test condition with the tightest end seal. The test element does not produce cross-coupled (stiffness and damping) coefficients.

2. The direct damping and inertia coefficients increase with the static eccentricity (large static load) but not as pronounced as the predictions otherwise indicate.

3. The end seals aid to substantially amplify the damping coefficient generated by the test ISFD. A tightly sealed ends ISFD (b_1=0.28 mm) shows 22 more damping that the open ends ISFD for motions about the static center e=0.

4. The sealed ends ISFD generates larger added mass coefficient (M_{ISFD}) compared with the one obtained for the open ends ISFD. However, the added mass coefficient reduces as the end seal gap (b_1) decreases from 0.53 mm to 0.43 mm. The experimentally estimated virtual masses are of the same magnitude or larger than the physical mass of the test element (19 kg).

5. The ISFD with tightly sealed ends, gap $b_1 = 0.28$ mm $(< c)$, shows a significant hardening

stiffening effect (negative virtual mass). Rationale for this finding is unknown as the predictive model entirely misses the experimental outcome.

6. The tool ISFDFLEX® predicts well the damping coefficients, but largely under predicts the added mass coefficients.

In general the current results support the findings for direct damping found in a prior test campaign [6]. On the other hand, Delgado et al. [6] report a predicted virtual mass coefficient that is larger than the experimental force coefficient. Presently, the predicted added mass coefficients are significantly lower than those experimentally obtained.

Acknowledgements

Nomenclature

a	Bearing housing acceleration [m/s^2]
b_1	End seal axial clearance [m]
b_2	End seal radial clearance [m]
c	ISFD damping land clearance [m]
C_{i,j_ISFD}	ISFD film damping coefficient [N.s/m], $i, j = X, Y$
C_S	ISFD structure damping coefficient [N.s/m]
C_G	End seals (global) flow conductance [m^3/(s-Pa)]
C_{seal}	End seal flow conductance [m^2/(s-Pa)]
D	$D = 2R$, Journal diameter [m]
D_{ISFD}	ISFD film land diameter [m]
e	ISFD static eccentricity [-]
f_X, f_Y	Components of external excitation force [N]
$H_{i,j}$	Complex dynamic stiffness [N/m]
i	Imaginary unit
K_{i,j_ISFD}	ISFD film direct static stiffness [N/m]
K_S	ISFD structure static stiffness [N/m]
l_1	End seal radial width [m]
l_2	End seal axial width [m]
L	ISFD length [mm]
M_{i,j_ISFD}	ISFD film mass coefficients [N.s/m], $i, j = X, Y$
M_S	ISFD structure mass coefficients [N.s/m], $i, j = X, Y$
P_a, P_s	Ambient pressure and supply pressure [Pa]

$P_{X,Y}$	First order pressure [Pa]
Q	Supply oil flow rate [m^3/s]
Re_s	Re$_s$= $(\rho/\mu)\omega c^2$, squeeze film Reynolds numbers
R_o	Orifice flow resistance [Pa s/m^3]
R_f	Damper film land flow resistance [Pa s/m^3]
R_S	End seal flow resistance [Pa s/m^3]
X,Y	Bearing cartridge displacements [m]
μ	Oil viscosity [Pa.s]
ρ	Oil density [kg/m^3]
ω	Excitation frequency [Hz]
Θ	Angular coordinate [Deg]

Matrices and vectors

A	Absolute acceleration vector [m/s^2]
C	Damping matrix, **C = C$_S$ + C$_{ISFD}$** [N·s/m]
C$_S$	Structure damping coefficient
Z	Bearing housing displacement vector [m]
F	External excitation force vector [N]
H	**K-** ω^2 **M** + $i\,\omega$ **C.** System complex dynamic stiffness matrix [N/m]
I	2x2 identity matrix.
K	System stiffness matrix, **K = K$_S$ + K$_{ISFD}$** [N/m]

Abbreviations

ISFD	Integral squeeze film damper
EDM	Electro discharge machining

Subscripts

in	inlet condition
S	Structure
_ISFD	ISFD

References

[1] San Andrés, L., 2012, *Modern Lubrication Theory*, "Squeeze Film Dampers (SFDs)," Notes 13, Texas A&M University Digital Libraries, http://oaktrust.library.tamu.edu/handle/1969.1/93197 [April 5th, 2019].

[2] De Santiago, O., Oliveras, J., and San Andrés, L., 1997, "Imbalance Response of a Rotor Supported on Open-ends Integral Squeeze Film Dampers," Research Progress Report to the turbomachinery Research Consortium, TRC-SFD-2-97, College Station, TX, May, 1997. (available at http://rotorlab.tamu.edu/tribgroup/default.htm).

[3] De Santiago, O., San Andrés, L., and Oliveras, J., 1998, "Imbalance Response of a Rotor Supported on Open-ends Integral Squeeze Film Dampers," ASME J. Eng. Gas Turb. Pwr., **121**(4), p. 718-724.

[4] Delgado, A., Cantanzaro, M., Mitaritonna, N., and Gerbet, M., 2011, "Identification of Force Coefficients in a 5-pad Tilting Pad Bearing with an Integral Squeeze Film Damper," 10th EDF/Pprime Poitiers Workshop, Poitiers, France, October 6-7.

[5] Agnew, J., and Childs, D., 2012, "Rotordynamic Characteristics of a Flexure Pivot Pad Bearing with an Active and Locked Integral Squeeze Film Damper," ASME Paper No. GT2012-68564.

[6] Ertas, B., Delgado, A., and Moore, J., 2018, "Dynamic Characterization of an Integral Squeeze Film Bearing Support Damper for a Supercritical CO_2 Expander," ASME J. Eng. Gas Turb. Pwr., **140**, p. 052501.

[7] San Andrés, L., Koo, B., and Jeung, S.-H., 2018, "Experimental Force Coefficients for Two Sealed Ends Squeeze Film Dampers (Piston Rings and O-rings): An Assessment of their Similarities and Differences," ASME J. Eng. Gas Turb. Pwr., **141** (2), p. 021024.

[8] Coghlan, D.M., 2014, "Static, Rotordynamic and Thermal Characteristics of a Four Pad Spherical-Seat Tilting Pad Journal Bearing with Four Methods of Directed Lubrication." M.S. Thesis, Texas A&M University, College Station, Texas.

[9] Delgado, A., and San Andrés, L., 2007, "A Model for Improved Prediction of Force Coefficients in Grooved Squeeze Film Dampers and Oil Seal Rings," ASME J. Tribol., 132, p. 032202.

Figure A-1 shows the setup for the measurement of the equivalent stiffness (k) of the S-shaped springs connecting a pad to the base ring. A pipe with a diameter 73.5 mm (smaller than the bearing diameter of 100 mm) and a wall thickness 6.7 mm supports the ISFD on just one bearing pad. A Hydraulic loader push the housing of the ISFD via a long bar. A load cell and a dial gauge record the applied force and the ensuing displacement. Fig. A-2 shows the ISFD with the end seals removed. The flexible bearing pads are fixed using brown shims. The direction of load applied on the pad straight upward.

Fig. A-3 shows the applied force vs. the measure displacement. The test is repeated 5 times. The symbols represent the average data and the error bars stand for variability (standard deviation). A linear curve fit of the data delivers a stiffness of $k= 38.8 \pm 5$ MN/m for the pair of elastic S-shaped structures holding a single pad. Note this stiffness is roughly 50% of the structure stiffness stated in the main text. This is expected as the overall structure stiffness (when all S-supports are active) should = [½ x Number of Pads (=4) x k] ~ 56.3 (±6) MN/m,
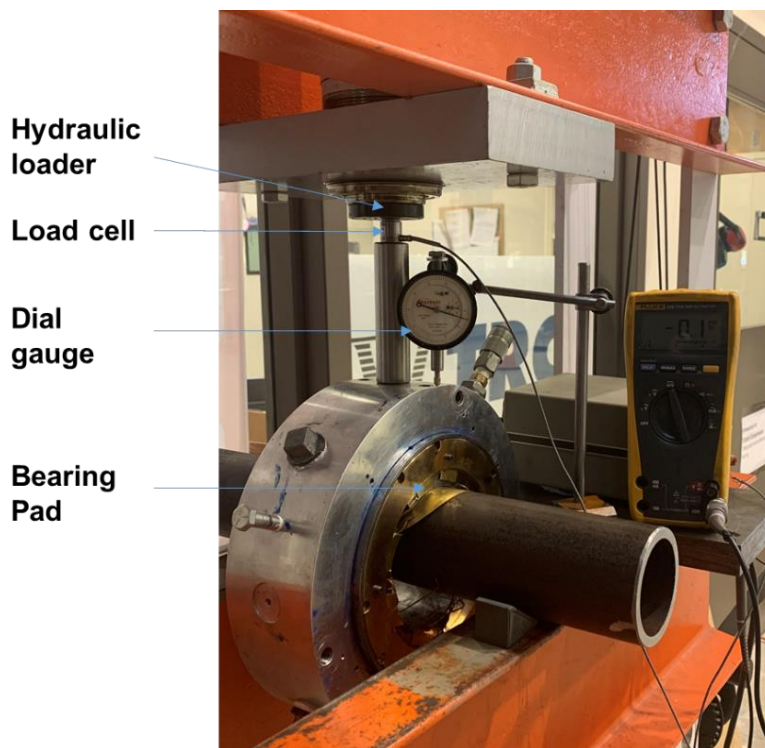

Fig. A- 1 Photograph with ad-hoc setup for the measurement of a pad S-shaped stiffness.

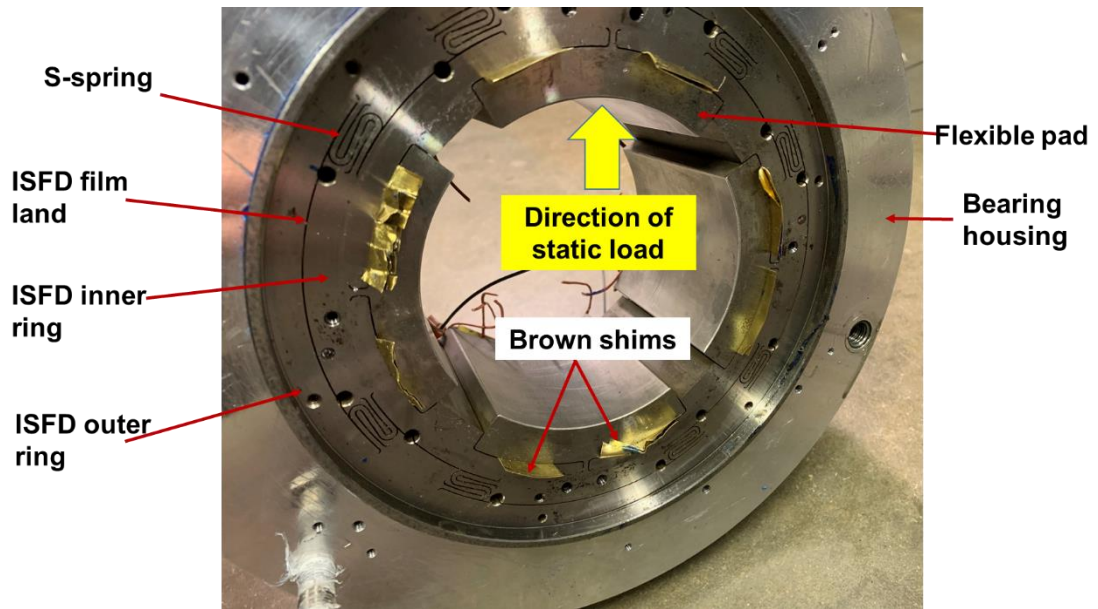**Fig. A- 2 ISD with affixed tilting pads with shims. Direction of static load shown**
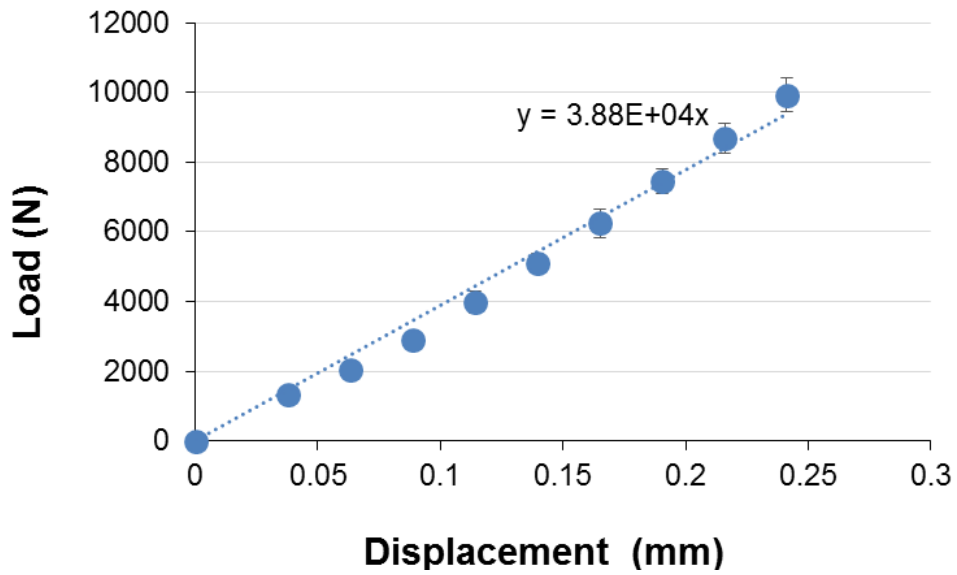

$y = 3.88E+04x$

Fig. A- 3 Static load versus displacement for one pad.

Appendix B Real and imaginary parts of dynamic complex stiffnesses for ISFD at static eccentricity *e/c* = 0 to 0.7

Figures B-1 and B-2 show the real and imaginary parts of the system complex dynamic stiffnesses (H) versus excitation frequency. The static eccentricity ratio (e/c) increases discretely from 0 to 0.7 due to an applied static load (hereby not reported for unknown reasons).

Note in Figure B-1, both $\text{Re}(H_{XX})$ and $\text{Re}(H_{YY})$ show a similar magnitude (~ 60 MN/m) for small excitation frequency, $\omega \rightarrow 0$ Hz, for all test conditions. The structure alone $\text{Re}(H)$ is denoted by the open symbols on the various graphs. Note the magnitude 60 MN/m is within the structure static stiffness K_S= 56.3 (±6) MN/m) reported in Fig. 10.

For end sealed configurations with gap (b_1) = 0. 53 mm and 0.43 mm (> c=0.356 mm), both $\text{Re}(H_{XX})$ and $\text{Re}(H_{YY})$ appear as quadratic functions of frequency, i.e. ~ ($K-\omega^2 M$), and distinctly show a virtual mass effect ($M>0$). Alas for the end sealed ISFD with b_1= 0.28 mm ($< c$), $\text{Re}(H_{XX})$ and $\text{Re}(H_{YY})$ increase with frequency! Rationale for this experimental result is yet to be found.

Figure B-2 depicts $\text{Ima}(H)_{XX, YY}$ versus frequency as the static eccentricity *(e/c)* changes from 0 to 0.7. The main finding is that $\text{Ima}(H)_{XX, YY}$ increases continuously with frequency. That is, $\text{Ima}(H) \sim C \omega$, represents a purely viscous effect.
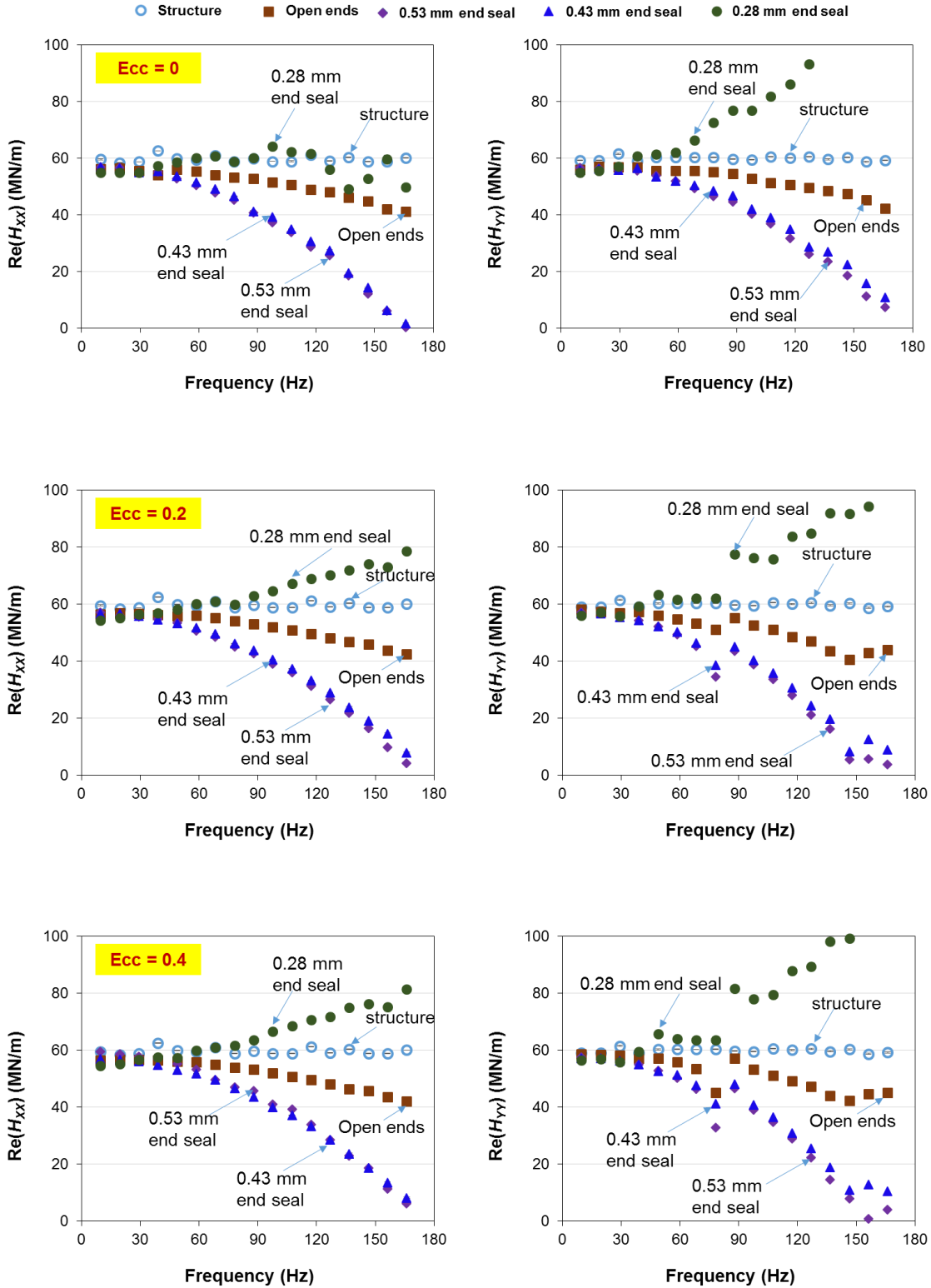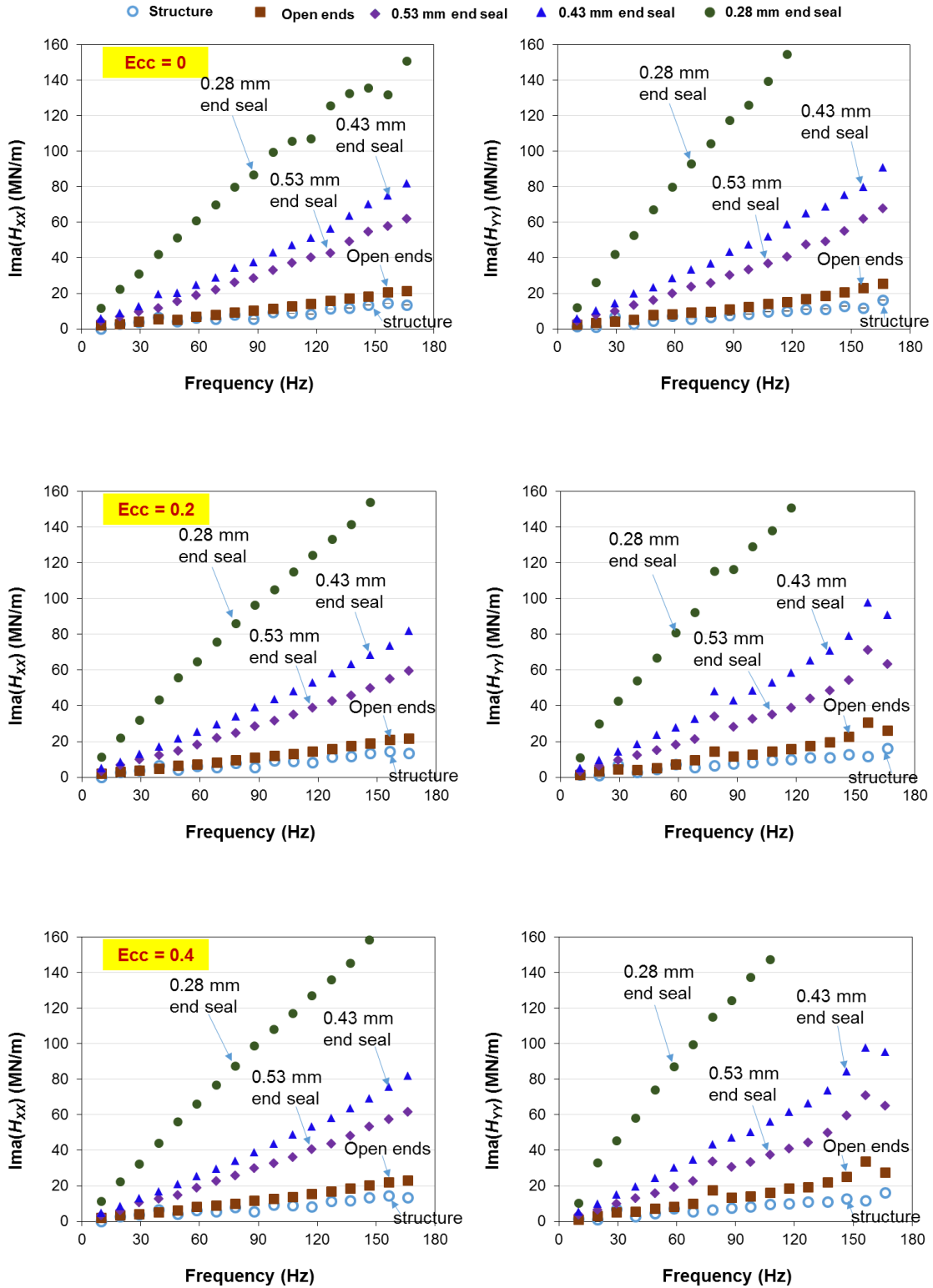
Fig. B- 1 (a) Real part of dynamic complex system stiffnesses, Re(HXX) and Re(HYY), vs excitation frequency. Open and end sealed ends. Centered and off-centered static eccentricity (e/c=0, 0.2, 0,4). Oil flow rate 9.5 L/min.
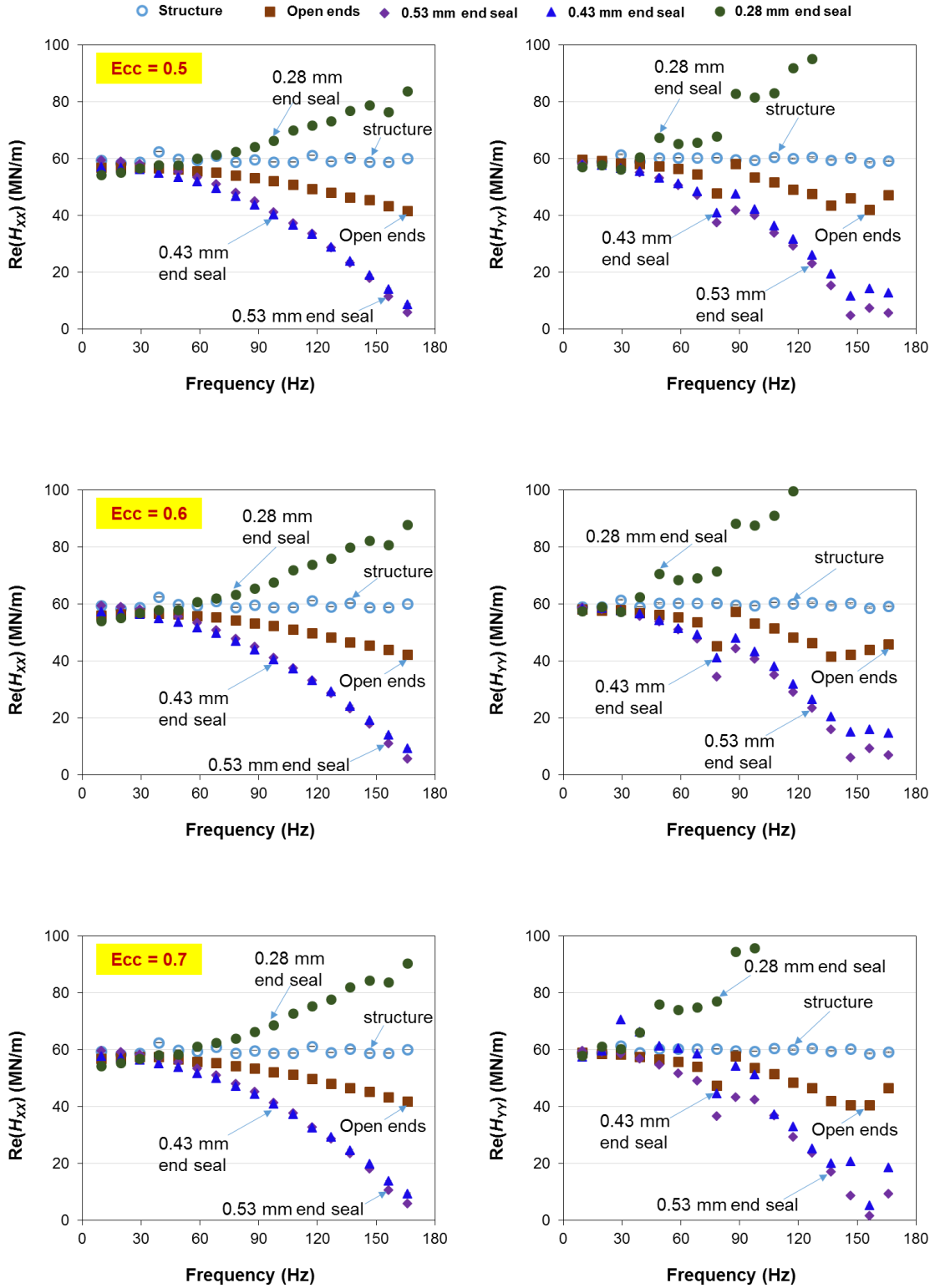
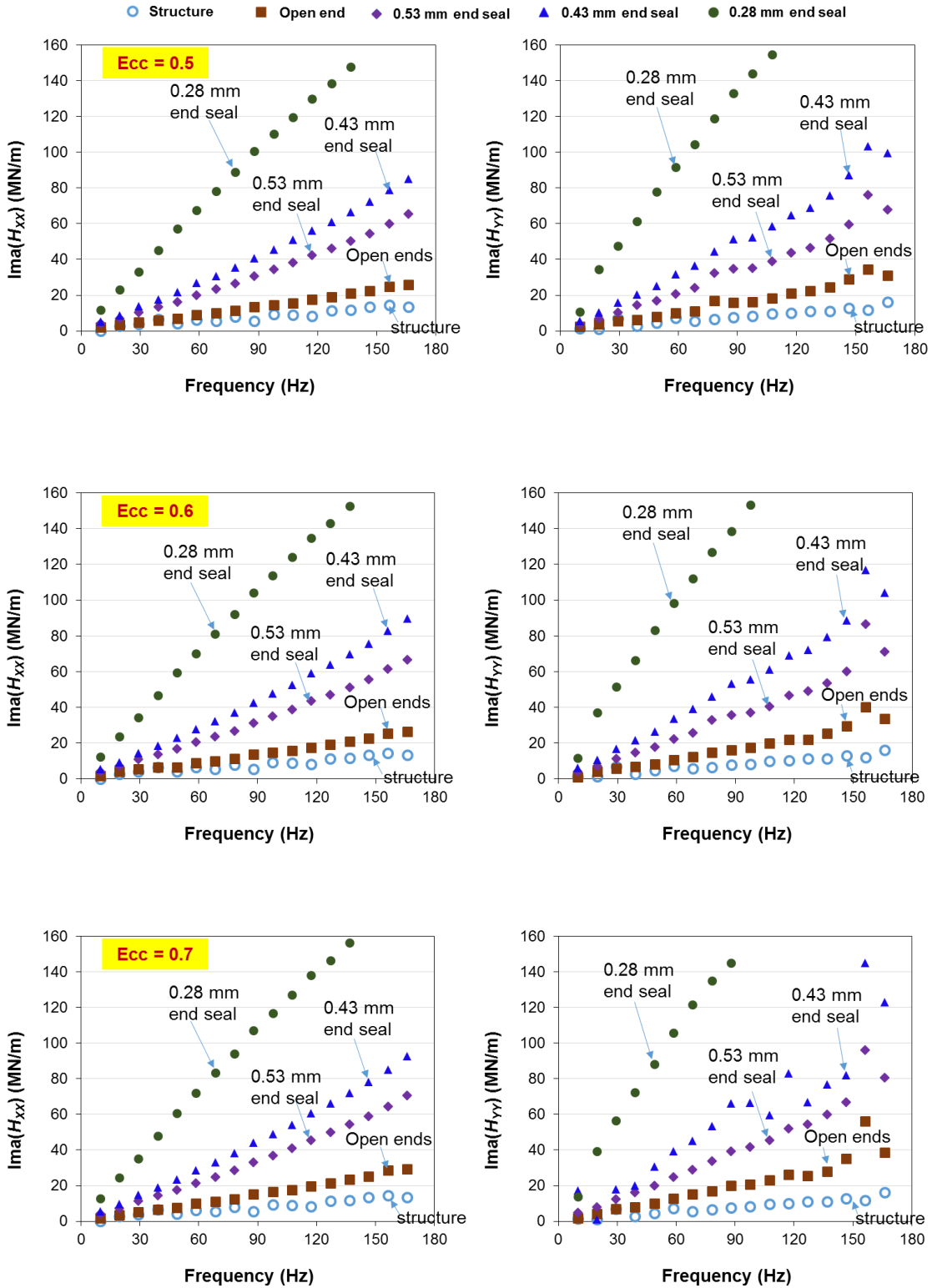**Fig. B-1 (b) Real part of dynamic complex system stiffnesses, Re(H_{XX}) and Re(H_{YY}), vs excitation frequency. Open and end sealed ends. Centered and off-centered static eccentricity (e/c=0, 0.5, 0.6, 0.7). Oil flow rate 9.5 L/min.**

Fig. B- 2 (a) Imaginary part of dynamic complex system stiffnesses, Ima(HXX) and Ima(HYY), vs excitation frequency. Open and end sealed ends. Centered and off-centered static eccentricity (e/c=0, 0.2, 0,4). Oil flow rate 9.5 L/min.

Fig. B-2 (b) Imaginary part of dynamic complex system stiffnesses, Ima(H_{XX}) and Ima(H_{YY}), vs excitation frequency. Open and end sealed ends. Centered and off-centered static eccentricity (e/c=0.5, 0.6, 0.7). Oil flow rate 9.5 L/min.

Appendix C Graphic user interface (GUI) for ISFD predictive tool

Figure C1 displays an example of the main worksheet in the GUI based on Excel. The predictive tool is named as ISFDflex®. A user can specify the damper geometry and fluid properties. The damper geometry includes the inlet and outlet boundary conditions, the number of feedholes, circumferential end types, and end seal coefficients (~0 for fully sealed ends and ~∞ for open ends). The structural stiffness coefficient (K_s) is for one S-spring structure.

There are two analysis types, (1) static eccentricity and (2) static load. For a (1) static eccentricity option, the program evaluates the clearance from the specified static load (X,Y) and structure stiffness. The Fortran based numerical model solves the perturbed pressure fields and delivers the damper force coefficients, see Eq. (4). For a (2) static load option, the code requires a list of static loads. From the specified static loads and structural properties, the code determines the static offset or eccentricity of the journal and then produces the damper force coefficients.
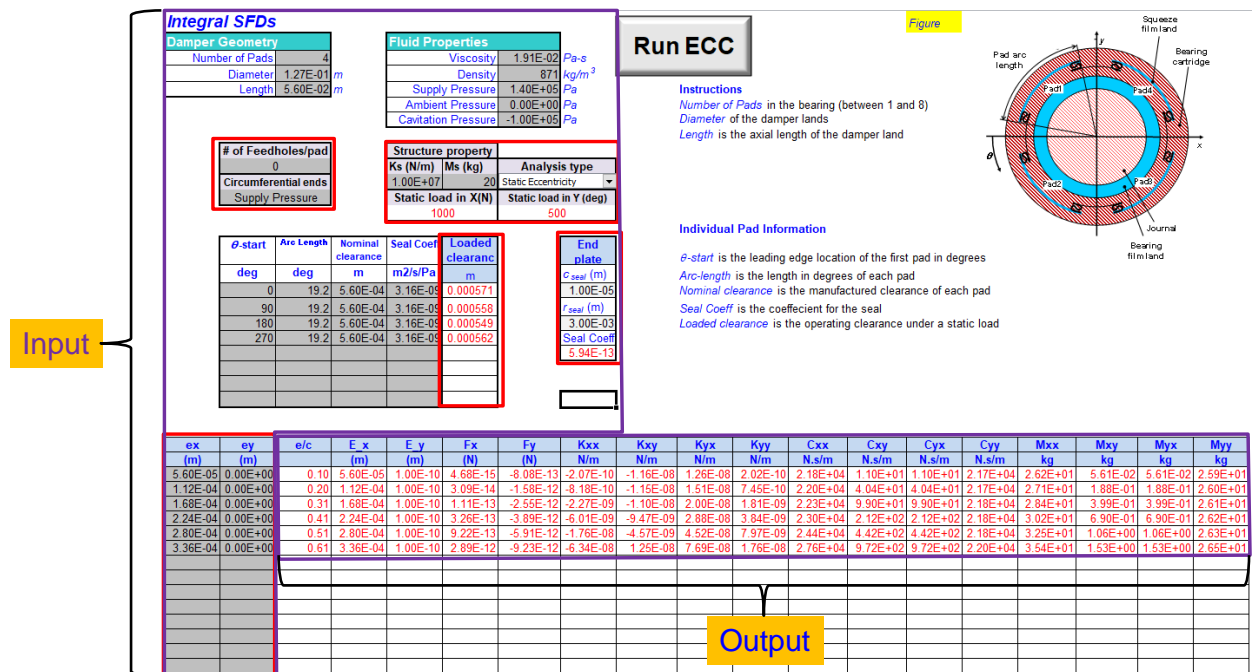

Figure C1. Main worksheet of GUI for ISFDflex®.